Physics prospects of the Jinping neutrino experiment

2017 Chinese Phys. C 41 023002

(http://iopscience.iop.org/1674-1137/41/2/023002)

Physics prospects of the Jinping neutrino experiment *

John F. Beacom[1] Shaomin Chen (陈少敏)[2;1)] Jianping Cheng (程建平)[2] Sayed N. Doustimotlagh [2]
Yuanning Gao (高原宁)[2] Guanghua Gong (龚光华)[2] Hui Gong (宫辉)[2] Lei Guo (郭磊)[2]
Ran Han (韩然)[3] Hong-Jian He (何红建)[2] Xingtao Huang (黄性涛)[4] Jianmin Li (李荐民)[2]
Jin Li (李金)[2] Mohan Li (李默涵)[2] Xueqian Li (李学潜)[5] Wei Liao (廖玮)[6]
Guey-Lin Lin (林贵林)[7] Zuowei Liu (刘佐伟)[2] William McDonough[8] Ondřej Šrámek[9]
Jian Tang (唐健)[10] Linyan Wan (万林焱)[2] Yuanqing Wang (王元清)[11] Zhe Wang (王喆)[2;2)]
Zongyi Wang (王综轶)[11] Hanyu Wei (魏瀚宇)[2] Yufei Xi (习宇飞)[12] Ye Xu (徐晔)[13]
Xun-Jie Xu (许勋杰)[2] Zhenwei Yang (杨振伟)[2] Chunfa Yao (姚春发)[14] Minfang Yeh [15]
Qian Yue (岳骞)[2] Liming Zhang (张黎明)[2] Yang Zhang (张洋)[2] Zhihong Zhao (赵志宏)[11]
Yangheng Zheng (郑阳恒)[16] Xiang Zhou (周详)[17] Xianglei Zhu (朱相雷)[2] Kai Zuber [18]

[1] Dept. of Physics, Dept. of Astronomy, and CCAPP, The Ohio State University, Columbus, OH 43210
[2] Department of Engineering Physics, Tsinghua University, Beijing 100084
[3] Science and Technology on Reliability and Environmental Engineering Laboratory, Beijing Institute of Spacecraft Environment Engineering, Beijing 100094
[4] School of Physics, Shandong University, Jinan 250100
[5] School of Physics, Nankai University, Tianjin 300371
[6] Institute of Modern Physics, East China University of Science and Technology, Shanghai 200237
[7] Institute of Physics, National Chiao-Tung University, Hsinchu
[8] University of Maryland, College Park, Maryland 20742
[9] Department of Geophysics, Faculty of Mathematics and Physics, Charles University in Prague, Prague
[10] School of Physics, Sun Yat-Sen University, Guangzhou 510275
[11] Department of Civil Engineering, Tsinghua University, Beijing 100084
[12] Institute of Hydrogeology and Environmental Geology, Chinese Academy of Geological Sciences, Shijiazhuang 050061
[13] Fujian University of Technology, Fujian 350118
[14] Department of Structural Steels, China Iron & Steel Research Institute Group 100081
[15] Brookhaven National Laboratory, Upton, New York 11973
[16] School of Physical Sciences, University of Chinese Academy of Sciences, Beijing 100049
[17] School of Physics and Technology, Wuhan University, Wuhan 430072
[18] Institut für Kern- und Teilchenphysik, Technische Universität Dresden, Dresden 01069

Abstract: The China Jinping Underground Laboratory (CJPL), which has the lowest cosmic-ray muon flux and the lowest reactor neutrino flux of any laboratory, is ideal to carry out low-energy neutrino experiments. With two detectors and a total fiducial mass of 2000 tons for solar neutrino physics (equivalently, 3000 tons for geo-neutrino and supernova neutrino physics), the Jinping neutrino experiment will have the potential to identify the neutrinos from the CNO fusion cycles of the Sun, to cover the transition phase for the solar neutrino oscillation from vacuum to matter mixing, and to measure the geo-neutrino flux, including the Th/U ratio. These goals can be fulfilled with mature existing techniques. Efforts on increasing the target mass with multi-modular neutrino detectors and on developing the slow liquid scintillator will increase the Jinping discovery potential in the study of solar neutrinos, geo-neutrinos, supernova neutrinos, and dark matter.

Keywords: CJPL, Jinping neutrino experiment, solar neutrino, geo-neutrino, supernova neutrino

PACS: 95.85.Ry, 14.60.Pq, 26.65.+t **DOI:** 10.1088/1674-1137/41/2/023002

Received 13 September 2016, Revised 26 October 2016

∗ Supported by the National Natural Science Foundation of China (11235006, 11475093, 11135009, 11375065, 11505301, and 11620101004), the Tsinghua University Initiative Scientific Research Program (20121088035, 20131089288, and 20151080432), the Key Laboratory of Particle & Radiation Imaging (Tsinghua University), the CAS Center for Excellence in Particle Physics (CCEPP), U.S. National Science Foundation Grant PHY-1404311 (Beacom), and U.S. Department of Energy under contract DE-AC02-98CH10886 (Yeh).

1) E-mail: chenshaomin@tsinghua.edu.cn (corresponding author)
2) E-mail: wangzhe-hep@tsinghua.edu.cn (corresponding author)

In this paper, we present the physics prospects of the Jinping neutrino experiment [1]. Section 1 briefly introduces the underground laboratory. Section 2 describes the detector concept. Sections 3–7 give the sensitivity studies for solar neutrinos, geo-neutrinos, supernova burst neutrinos, supernova relic neutrinos and dark matter, respectively. Section 8 gives a brief summary.

1 Experimental site

1.1 Overview

The China Jinping Underground Laboratory (CJPL) [2] is located in Sichuan province, China, 28.2°N, 101.7°E and 2400 meters under Jinping mountain.

The first phase of the Jinping laboratory (CJPL-I) was constructed in the middle of the traffic tunnels at the end of 2009. Two dark matter experiments, CDEX [3] and PandaX [4] are now running at CJPL-I. The second phase of the Jinping laboratory (CJPL-II) started at the end of 2014. Four 150-m long tunnels have been constructed to provide space for more underground experiments [5].

We propose to build two neutrino detectors in CJPL-II, with a total fiducial target mass of 2000 tons for solar neutrino physics and, equivalently, 3000 tons for geo-neutrino and supernova neutrino physics. The initial plan is to adopt the liquid-scintillator technique as the baseline design, with the capacity of extension to a slow scintillator detector.

1.2 Rock radioactivity

The radioactivity of the rock in Jinping tunnel was measured [6] and the results are shown in Table 1 together with the measurements from Sudbury [7], Gran Sasso [8], and Kamioka [9] underground laboratories.

Table 1. Radioactivity contamination in Bq/kg for some underground laboratories.

site	^{238}U	^{232}Th	^{40}K
Jinping	1.8±0.2 (^{226}Ra)	<0.27	<1.1
Sudbury	13.7±1.6	22.6±2.1	310±40
Gran Sasso hall A	116±12	12±0.4	307±8
Gran Sasso hall B	7.1±1.6	0.34±0.11	7±1.7
Gran Sasso hall C	11±2.3	0.37±0.13	4±1.9
Kamioka	∼12	∼10	∼520

1.3 Cosmic-ray muon flux

According to the in-situ measurement [10], the muon flux is as low as $(2.0 \pm 0.4) \times 10^{-10}/(\mathrm{cm}^2 \cdot \mathrm{s})$. A comparison with other underground labs can be seen in Fig. 1 [10, 11]. Cosmic-ray muon induced radioactive isotopes are extremely dangerous backgrounds for low-energy neutrino experiments and are therefore expected to be significantly suppressed at Jinping.

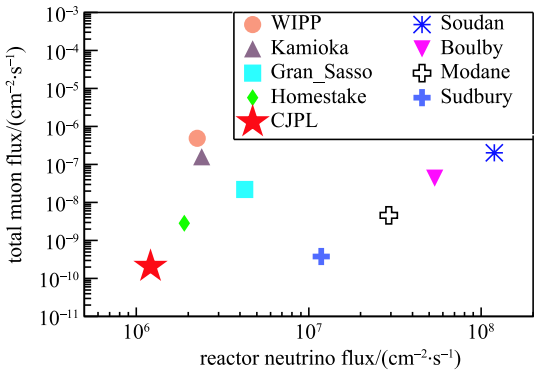

Fig. 1. (color online) Muon flux vs reactor neutrino background flux for various underground labs in the world.

1.4 Reactor neutrino background

Jinping is also far away from all the nuclear power plants [12] in operation and under construction. A world map with all nuclear power plants and SNO, Gran Sasso, Kamioka, and Jinping laboratories is shown in Fig. 2. A reactor background flux comparison with these laboratories is shown in Fig. 1. The reactor electron antineutrino background at Jinping is rather low and will be explained in detail in later sections.

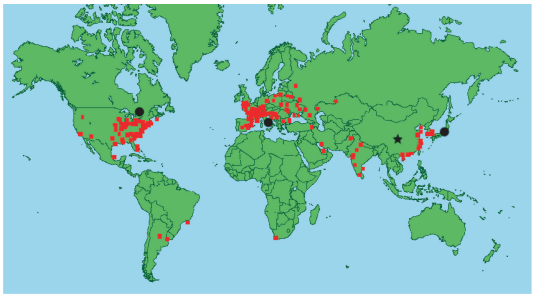

Fig. 2. (color online) World map with all the nuclear power plants in operation and under construction. SNO, Gran Sasso, Kamioka and Jinping laboratory locations are also marked.

2 Detector concept

With the primary physics goals for low-energy neutrinos, the Jinping detector design follows the structure adopted by the recent underground neutrino experiments, and it will also consider the unique features of the low environmental backgrounds and the tunnel structure.

Target mass is a key factor of the proposed neutrino experiment and a few constraints must be considered to

reach the level of target mass requirement. In addition, graded shielding is necessary to reach a radioactive clean central region.

1) The deep overburden limits both the tunnel size and shape, putting a constraint on the target volume for a single detector. A thin and long detector is very poor for physics performance.

2) The attenuation length is about 20 meters for liquid scintillators. A detector should not have a dimension significantly larger than this length.

3) Water shielding in the outer layer was used in previous experiments to detect cosmic-ray muons and shield the detector from neutrons and radiative gammas in the surrounding rock, steel structure, and PMTs. The minimal thickness is around 1–2 meters.

4) A central fiducial volume is necessary to reject background events in the outer layer of the target region, which is usually from the gamma backgrounds on the target material vessel.

5) Cost and risk for any large amount of civil construction and detector construction.

In this section, we give a preliminary plan for the neutrino detectors. A preliminary study from a test-stand is also shown to demonstrate the possible separation between Cherenkov and scintillation light. Considering the current level of technology and expected development, we also give some thought to the electronics used to precisely read out the waveform from photomultiplier tubes (PMTs).

2.1 Experimental hall layout and neutrino detector

At CJPL-II, two cylindrical caverns have already been planned, each around 20 m in diameter and 24 m in height.

A conceptual design for a cylindrical neutrino detector can be seen in Fig. 3. A spherical inner vessel is also an option. The central vessel is made of acrylic, and the height and diameter of the cylinder are both 14 meters. The vessel is filled with the target material, which can be either a regular liquid scintillator or a slow liquid scintillator. The fiducial volume is defined by a cylinder of 11.2 m diameter and 11.2 m height, and the fiducial mass is 1 kiloton assuming the target material density is 0.9 g/cm^3.

The central vessel will be sealed and surrounded with pure water. Scintillation and Cherenkov light originating from neutrino interactions with the target material in the central region will be collected by the PMTs. These PMTs will be mounted on a supporting stainless steel structure, and will be kept 2–3 m away from the central vessel to shield from gammas. The outermost layer of the detector is a low radioactive stainless steel tank 20 m in both diameter and height, which hosts the central vessel, PMTs, supporting structure, and pure water.

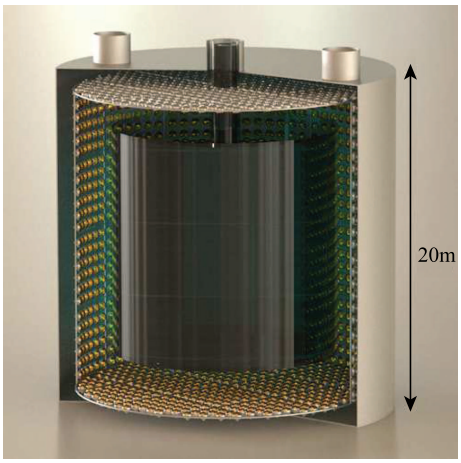

Fig. 3. (color online) The conceptual design for a cylindrical neutrino detector at Jinping. Two detectors are needed to reach the desired mass requirement.

With two neutrino detectors, the total fiducial volume will be about 2 kilotons for the solar neutrino studies, in which the detection process is neutrino-electron scattering. For the geo-neutrino and supernova neutrino studies, the equivalent fiducial mass can be extended to 3 kiloton, because the signal is from the inverse beta decay process, i.e. a prompt-delayed coincidence, and has a better rejection of background.

Such a design is considered as the most economic option when balancing the need of the fiducial mass and the dimensions of the CJPL-II tunnel. However, continuing studies incorporated with scintillator performance are ongoing to finalize the detector design.

2.2 Target material

We will use a liquid scintillator with sufficient light yield for our baseline design. We also consider using a slow liquid scintillator aiming at the separation between Cerenkov and scintillator light. Redundant measurements of a particle can be possible in this option. The prompt Cherenkov light can be used for the directional reconstruction of charged particles while the slow scintillation light can be used for the energy reconstruction of particles. Furthermore, Cherenkov light yield and scintillation light yield have different dependencies on particle momentum and can be exploited to identify gammas, electrons, muons, and protons.

2.2.1 Liquid scintillator

The light yield of liquid scintillator can be as high as $(1-2)\times10^4$ photons/MeV, which is sufficient for the energy resolution required in later sections.

2.2.2 Slow liquid scintillator

Slow liquid scintillator could be water based or oil based, which is still under development. Linear alkyl benzene (LAB) is one important ingredient for the water-based liquid scintillator (WbLS) [13, 14]. With a 20 liter container in a small test-stand [15], we measured the time profile of scintillation light in the LAB and tested the waveform separation between Cherenkov and scintillation light. As shown in Fig. 4, a clear separation between the Cherenkov (prompt component) and scintillation (slow component) light can be achieved. The yield of scintillation light was estimated to be 1×10^3 photons/MeV. More effort is needed to balance the fast and slow components with increasing light-yield.

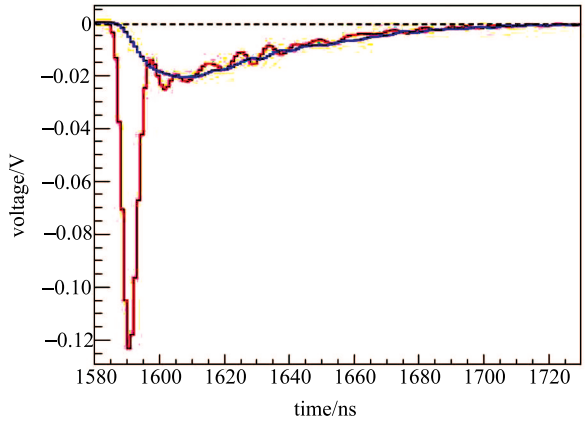

Fig. 4. (color online) Average waveforms of the Cherenkov+scintillation (red) and scintillation-only (blue) light in LAB.

2.3 Electronics

Because of the different fine timing structures in the slow liquid scintillator detector, a dedicated electronics system is needed to record the waveform output from the PMTs. This new feature can consequently be exploited to perform particle identification between gammas, electrons, and protons, for instance.

Waveform sampling with 1 GHz FLASH ADC (FADC) will be applied as the baseline technology for the Jinping neutrino experiment. Multi channels with different gains will be used to cover the dynamic range from 1 photon-electron (PE) to 100 PE.

For each PMT, a separate electronics module with a High Voltage generator, a base divider, an FADC sampler and a processing circuit will be installed at the end of each PMT in a water tight housing. The signal from a PMT does not need to pass through any coaxial cable which may degrade the signal quality and timing resolution. The reliability of the circuit and the housing structure is a major design challenge.

Each PMT works in self-trigger mode: whenever a signal level goes beyond a given threshold, the sample data in a designed readout window around the over-threshold points will be stored and transferred. The window size is adjustable up to a few micro-seconds. All the electronics contain synchronized time-tick counters for aligning sample fragments among PMTs.

Out of the water, the back-end electronics will provide the data acquisition, clock synchronization and control service. The PMT electronics and back-end electronics will be connected via multi-pair twist cables which will carry the low voltage power supply, dedicated clock/time signal, upstream and downstream data links. An encoding algorithm with variable lengths will be applied to the data stream to reduce the bandwidth requirement.

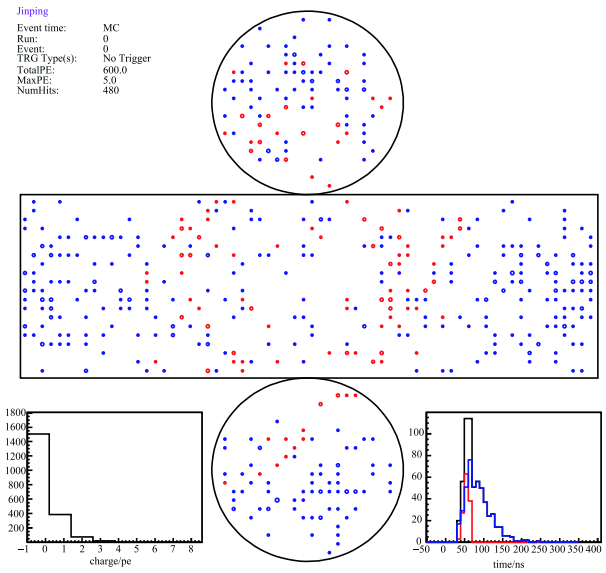

Fig. 5. (color online) An event display of a 7 MeV electron simulation in a cylindrical detector filled with LAB. Each circle indicates a PMT with at least one photo-electron (PE) detected. The red circles are for prompt Cherenkov radiation, and the blue ones are for the scintillation light, where the Cherenkov or scintillation identification is based on MC truth. The bottom-left panel is for the distribution of the number of PEs for all the PMTs, and the bottom-right panel is for the time distribution. A Cherenkov ring is visible in this plot.

2.4 Simulation studies

Preliminary simulation studies have been started to optimize the detector design to take the advantage of the Jinping laboratory environment and achieve the

physics goals. The following work was done with the Geant4 [16, 17] simulation package together with the customized geometry, light emission model, PMT response, etc. Figure 5 shows an event display for a 7 MeV electron, which can be produced via the neutrino-electron scattering in LAB according to our measurement. For demonstration purposes, we use different colors for the Cherenkov and Scintillation light.

3 Solar neutrinos

3.1 Introduction

Particles from sources at cosmic distances are of great interest. Neutrinos, as a stellar probe, have extremely low interaction cross sections. Unlike gammas, optical photons and protons, neutrinos can easily reach our detectors without being interrupted by matter on their paths. The original status, i.e. energy and direction, can therefore be maximally maintained, except that the neutrino flavors will oscillate among the three families of neutrinos, and consequently information about the initial interactions of neutrino productions can be probed. The attributes of neutrinos make them powerful probes of the deep interiors of sources like the Sun, providing ways to test models of solar evolution along with neutrino oscillation.

3.1.1 Solar models

Solar models, neutrino theories, and solar neutrino experiments have developed rapidly over the past half a century. This remarkable history has been documented in Refs. [18–21] and references therein. Nowadays the Sun is described by the Standard Solar Model (SSM) [22, 23], which relies on about 20 parameters.

- The first group of parameters are the current solar age, luminosity, mass, and radius.
- The primordial abundances of key elements, He, C, N, O, Ne, Mg, Si, S, Ar, and Fe.
- The cross-sections of nuclear reactions, including p(p, $e^+\nu_e$)d, d(p, γ)^{3}He, ^{3}He(^{3}He, 2p)^{4}He, ^{3}He(^{4}He, γ)^{7}Be, ^{3}He(p, $e^+\nu_e$)^{4}He, ^{7}Be(e^-, ν_e)^{7}Li, p(e^-p, ν_e)d, ^{7}Be(p, γ)^{8}B, ^{14}N(p, γ)^{15}O.

The evolution starts with a cluster of homogeneous gas of H, He, C, N, etc. Nuclear fusion reactions burn H, He to heavier elements and emits gammas, electrons, positrons, etc. The Sun fuels itself by both the pp and CNO fusion processes, in which the pp-cycle contributes 99% of the total for energy production. The whole processes are constrained by the boundary conditions of the current solar status. The transport of energy in the central region is primarily through the inverse bremsstrahlung process of photons, and the calculated radiative opacity depends upon the chemical composition and the modeling of complex atomic processes. In the outer region, the energy is brought to the surface by convective motion. The interior of the Sun is assumed to be spherical symmetric and to be at the balance of gravity, radiation, and particle pressure.

The present composition of the solar surface is presumed to reflect the initial abundances of all of the elements that are as heavy as carbon [24]. These metal elements are assumed to be chemically homogeneous throughout the Sun, except for a minor correction due to diffusion. Suggestions have been made to argue the assumption of composition. CNO neutrino measurement could be a direct test of the solar-core metallicity [25, 26].

The nuclear reaction cross-sections are from theoretical calculations and/or terrestrial measurements [27, 28]. For example, the cross-section for the initial p(p, $e^+\nu_e$)d process is too low to be measured in a laboratory, and has to be calculated with nuclear physics theory. The ^{3}He(^{4}He, γ)^{7}Be cross-section is measured in the laboratory, and the result must be extrapolated to the solar Gamow peak with correct theoretical consideration. More experimental efforts on this regard can be found in LUNA [29], JUNA [30], and [31] etc.

Electron neutrinos can oscillate to muon and tau neutrinos in the three-flavor framework in vacuum or low electron-density material [32, 33]. However, this quantum ability of neutrinos is changed in the high electron-density environment in the Sun's interior, also known as the matter, Mikheyev-Smirnov-Wolfenstein (MSW) effect [34, 35].

The SSM describes the whole life of the Sun from the pre main-sequence time to the current day, even into the future. The study of solar neutrinos directly tests the theory of stellar evolution, nuclear energy generation, and neutrino oscillation. The knowledge of the Sun is critical to further understand stars in distant space.

3.1.2 Solar neutrino experiments

The first triumph of solar neutrino flux measurement was for the ν_e component detected using a ^{37}Cl detector at Homestake [36], but it was a big surprise that the measurement was only about 50% of the prediction. The following steady experimental efforts by SAGE (^{71}Ga detector) [37], GALLEX (^{71}Ga detector) [38], GNO (^{71}Ga detector) [39], Kamiokande (water Cherenkov detector) [40], and Super Kamiokande (water Cherenkov detector) [41] all confirmed the Homestake measurement. Later the SNO [42] experiment used a heavy water detector to make a measurement sensitive to all the flavors, whose neutral current scattering result agrees with the SSM prediction. Today we understand that electron neutrinos, ν_e, generated through the fusion processes oc-

curring inside the Sun may oscillate to other flavors, ν_μ or ν_τ, and this process is affected by the MSW effect in the surrounding dense materials in the Sun.

Recently the Borexino experiment successfully identified the low energy ^{7}Be, pep and pp solar neutrinos, and measured the fluxes in agreement with the SSM prediction when taking the oscillation into account [43]. A new era of precision measurement of the solar neutrino has begun.

3.1.3 Helioseismology

Solar oscillation was first found in Ref. [44] by studying the velocity shifts in absorption lines formed in the solar surface. The surface of the Sun is divided into patches which oscillate with velocity amplitudes of order 0.5 km s^{-1} and periods of order 5 minutes. This phenomenon can be used to deduce a precise sound speed profile in the Sun and correspondingly the density and pressure profile. Helioseismology is the other method that can be used to study the interior of the Sun.

3.1.4 Open Problems

The remaining issues for the properties of neutrinos and the solar model [45–47] are summarized below.

- Discovery of the missing solar neutrino components is expected from a more precise measurement [19, 25, 48]. CNO neutrinos are believed to dominate the fueling processes inside high temperature massive stars, but have not yet been observed by any neutrino experiment. Searching for CNO neutrinos from the Sun is the first practical approach, despite its relatively small flux. The hep neutrinos are also still missing from any experimental measurements.

- Precise measurements of all the solar neutrino components will provide not only a tighter constraint on the solar model, but also a high statistics observation of pp and others in real time, all of which might give completely new insights into the energy production and fluctuation of stars. In addition, a precise measurement of the solar neutrino flux could play a key role in the study of the following problems.

- Solution of the metallicity problem. As discussed in Ref. [49, 50], an improved solar model prediction is available with the input of the most up-to-date photospheric abundance of metals, which is 30% lower than earlier results. The new calculation based on the low metallicity assumption predicts lower fluxes for several neutrino components than those based on the previous high metallicity assumption. The next generation of solar neutrino experiments are expected to resolve the conflict.

  A precise measurement of the CNO neutrino is especially important for the metallicity problem [25, 26]. The relation of the solar neutrino fluxes and helioseismology can be seen in Fig. 6. The CNO neutrino flux predicted by the SSM has a direct dependence on the abundance of the metal elements than other components. The variance of metallicity will change the temperature, density and pressure profile and affect the fluxes of others indirectly.

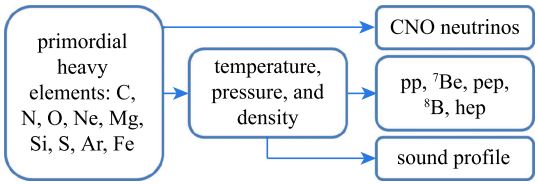

Fig. 6. (color online) The relation of solar neutrino fluxes and sound speed measurement of helioseismology.

- A full picture of the MSW effect in the solar electron neutrino oscillation. The oscillation of low energy ν_e, < 1 MeV, likely occurs in vacuum. As the neutrino energy increases, the MSW effect on solar neutrino oscillation emerges and becomes dominant due to the high electron density environment of the Sun's interior, and the transition of ν_e to the other flavors will eventually reach a maximum. However, this transition region from vacuum to matter is still poorly constrained by experiments [51–54].

- Precise measurements of θ_{12} and Δm^2_{21}. There is currently a 2σ tension in the Δm^2_{21} measurement between solar [55] and reactor measurements [56]. The Sun emits electron-neutrinos, while reactors emits electron-antineutrinos. Better measurements can be used to improve the measurement of the PMNS matrix and matter effect, and provide a test of CPT invariance as well. A more precise value of θ_{12} will help to define a better lower edge of the inverted neutrino mass hierarchy, and is thus important for neutrinoless double beta decay experiments in the future.

- Observation of ν_e regeneration inside the Earth. The Earth should in principle have a terrestrial matter effect on solar neutrinos. A regeneration of these neutrinos will give rise to a flux asymmetry for electron flavor solar neutrinos during the daytime and the nighttime [57, 58]. An indication of the day-night asymmetry has already been observed with a 2.7σ significance at Super Kamiokande [59].

- Probing the sub-leading effects in addition to neutrino oscillation [51, 54]. The Sun serves as an ideal neutrino source to probe for new physics, especially for those through a secondary effect of the standard scheme. In addition, the expected upturn behavior has not been observed yet for the solar neutrino oscillation from the matter to the vacuum effect. This has left a lot of space for non-standard neutrino interactions. Other interesting topics can also be studied with solar neutrinos, such as new neutrino states, sterile neutrinos, effects of violation of fundamental symmetries, new dynamics of neutrino propagation, and probes of space and time.

The rest of the section is arranged as follows. Section 3.2 introduces the simulation setup for the sensitivity study, including neutrino oscillation probability, solar neutrino model, detector configuration, etc. Section 3.3 addresses the systematics which can affect the studies of the solar model and MSW effects. Section 3.4 gives the sensitivity for identifying each solar neutrino component. Sections 3.5, 3.6 and 3.7 discuss the potentials for studying the transition of vacuum-matter oscillation, day-night asymmetry, and the test of high and low metallicity models, respectively.

3.2 Simulation study

A simulation study was done with some default settings for Jinping, including the expected signal and background levels, energy resolution, target mass, and live time, in order to evaluate the sensitivity for each physics topic.

3.2.1 Solar neutrino model

The neutrino energy spectra for all the solar neutrino components were taken from Ref. [22]. The average neutrino flux predictions on Earth without the oscillation effect are from Ref. [50, 60] for the high and low metallicity hypotheses, respectively. The correlations between the neutrino components estimated in Ref. [61] were used in the study. The spectra with the high metallicity flux prediction are shown in Fig. 7 and all the numerical values are listed in Table 2.

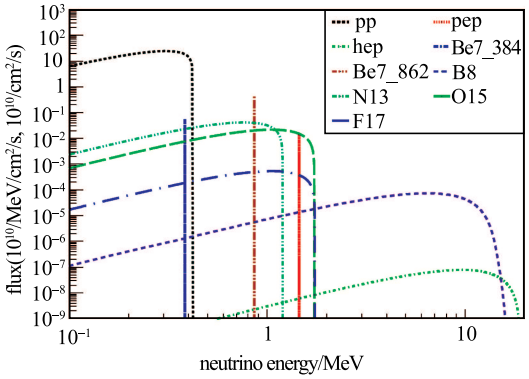

Fig. 7. (color online) Solar neutrino energy spectra and fluxes with the high metallicity hypothesis, where the unit for continuous spectra is 10^{10}/MeV/cm^2/s, and for discrete lines is 10^{10}/cm^2/s.

Table 2. Theoretical predictions for solar neutrino fluxs and errors without oscillation based on the high and low metallicity hypotheses [50, 60]. The production branching ratios for the 0.38 and 0.86 MeV ^{7}Be lines are 0.1052 and 0.8948, respectively.

	E_{Max} or E_{Line}/ MeV	flux (GS98) high metallicity/ ($\times10^{10}$s^{-1}cm^{-2})	flux (AGS09) low metallicity/ ($\times10^{10}$s^{-1}cm^{-2})
pp	0.42	$5.98(1\pm0.006)$	$6.03(1\pm0.006)$
^{7}Be	0.38	$0.053(1\pm0.07)$	$0.048(1\pm0.07)$
	0.86	$0.447(1\pm0.07)$	$0.408(1\pm0.07)$
pep	1.45	$0.0144(1\pm0.012)$	$0.0147(1\pm0.012)$
^{13}N	1.19	$0.0296(1\pm0.14)$	$0.0217(1\pm0.14)$
^{15}O	1.73	$0.0223(1\pm0.15)$	$0.0156(1\pm0.15)$
^{17}F	1.74	$5.52\times10^{-4}(1\pm0.17)$	$3.40\times10^{-4}(1\pm0.17)$
^{8}B	15.8	$5.58\times10^{-4}(1\pm0.14)$	$4.59\times10^{-4}(1\pm0.14)$
hep	18.5	$8.04\times10^{-7}(1\pm0.30)$	$8.31\times10^{-7}(1\pm0.30)$

3.2.2 Oscillation probability

The propagation path of solar neutrinos from the Sun to the Earth can be divided into three parts: 1) from the inner core to the surface of the Sun; 2) from the surface of the Sun to the surface of the Earth; 3) the path through the Earth during the nighttime.

The survival probability of solar electron neutrinos with energy E_ν from the inner core to the surface of the Sun must include the matter effect [34, 35] and can be approximated by the following formula [62, 63],

$$P_{ee}^{\odot} = \cos^4\theta_{13}\left(\frac{1}{2}+\frac{1}{2}\cos2\theta_{12}^{M}\cos2\theta_{12}\right), \tag{1}$$

where the mixing angle in matter is

$$\cos2\theta_{12}^{M} = \frac{\cos2\theta_{12}-\beta}{\sqrt{(\cos2\theta_{12}-\beta)^2+\sin^2 2\theta_{12}}}, \tag{2}$$

with

$$\beta = \frac{2\sqrt{2}G_{\rm F}\cos^2\theta_{13}n_{\rm e}E_\nu}{\Delta m_{12}^2}, \tag{3}$$

where $G_{\rm F}$ is the Fermi coupling constant and $n_{\rm e}$ is the density of electrons in the neutrino production place of the Sun. The calculation is done under the assumption

of adiabatic evolution [64], so that the density of electrons varies slowly and does not cause any exchange among the mass eigenstates after being created. For the solar case initially only ν_e's are produced by the fusion processes. With $\sin^2\theta_{12}$=0.307, $\sin^2\theta_{13}$=0.0241, $\Delta m^2_{12} = 7.54\times10^{-5}$ eV^2, and $n_e = 6\times10^{25}$/cm^3 [65] in the inner core of the Sun, the survival probability of ν_e as a function of neutrino energy was obtained, without considering the generation of radius distribution of each component. Correspondingly the appearance probability of ν_μ and ν_τ is

$$P^{\odot}_{e\mu(\tau)} = 1 - P^{\odot}_{ee}. \quad (4)$$

The second part is the disappearance probability for the propagation from the surface of the Sun to the surface of the Earth. The mass eigenstates of neutrinos emerging from the surface of the Sun are treated as decoherent [66] due to the sizable width of the energy spectrum of each neutrino component, even for ^{7}Be neutrinos [67]. The amplitudes of all the mass eigenstates keep unchanged and decoherent all the way to the Earth. The fluxes per unit area only decrease by a factor of the Earth-Sun distance squared with a percent-level annual modulation effect due to the eccentric orbit of the Earth. The above oscillation probability $P^{\odot}_{ee}$ is sufficient for most studies [68].

3.2.3 Elastic scattering cross section

The neutrino electron elastic scattering process will be used to detect solar neutrinos. The scattered electron's energy and direction can be measured and used to derive the incoming neutrino energy and direction. The differential scattering cross-sections as a function of the kinetic energy of the recoil electron, T_e, and neutrino energy, E_ν, in the electron rest frame can be written, for example, in Ref. [69] as:

$$\frac{d\sigma(E_\nu,T_e)}{dT_e} = \frac{\sigma_0}{m_e}\left[g_1^2 + g_2^2\left(1-\frac{T_e}{E_\nu}\right)^2 - g_1 g_2\frac{m_e T_e}{E_\nu^2}\right], \quad (5)$$

with

$$\sigma_0 = \frac{2G_F^2 m_e^2}{\pi} \simeq 88.06\times10^{-46}\text{cm}^2, \quad (6)$$

where m_e is the electron mass. Depending on the flavor of the neutrino, g_1 and g_2 are:

$$\begin{aligned} g_1^{(\nu_e)} &= g_2^{(\bar\nu_e)} = \frac{1}{2} + \sin^2\theta_W \simeq 0.73, \\ g_2^{(\nu_e)} &= g_1^{(\bar\nu_e)} = \sin^2\theta_W \simeq 0.23, \end{aligned} \quad (7)$$

where θ_W is the Weinberg angle, then for $\nu_{\mu,\tau}$ they are

$$\begin{aligned} g_1^{(\nu_{\mu,\tau})} &= g_2^{(\bar\nu_{\mu,\tau})} = -\frac{1}{2} + \sin^2\theta_W \simeq -0.27, \\ g_2^{(\nu_{\mu,\tau})} &= g_1^{(\bar\nu_{\mu,\tau})} = \sin^2\theta_W \simeq 0.23. \end{aligned} \quad (8)$$

The differential cross-section for ν_e electron scattering as a function of T_e and the cosine angle between the recoiling electron and initial neutrino direction are shown in Fig. 8. The directional information will be less useful when the energy of solar neutrino becomes smaller.

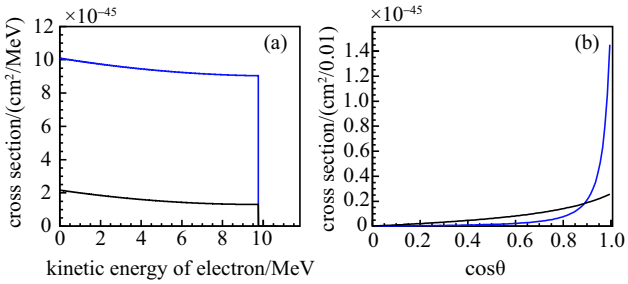

Fig. 8. (color online) (a) the differential cross section for the scattering as a function of the kinetic energy of recoil electron for a 10 MeV ν_e (blue) and $\nu_{\mu,\tau}$ (black); (b) the distribution of the cosine angle between the recoiling electron and initial neutrino direction for a 10 MeV ν_e (blue) and a 1 MeV ν_e (black).

3.2.4 Detectable electron spectrum

Since the observed spectrum of electron kinetic energy contains all the contributions from electron-, muon- and tau-neutrinos, the electron kinetic energy spectrum becomes

$$\begin{aligned} R_\nu = & N_e\Phi_\nu\int dE_\nu\frac{d\lambda}{dE_\nu}\int\left\{\frac{d\sigma_e(E_\nu,T_e)}{dT_e}P_{ee}(E_\nu)\right. \\ & \left.+\frac{d\sigma_{\mu,\tau}(E_\nu,T_e)}{dT_e}[1-P_{ee}(E_\nu)]\right\}dT_e, \end{aligned} \quad (9)$$

where N_e is the number of electrons in the target, Φ_ν is the neutrino flux of the Sun, $d\lambda/dE_\nu$ is the differential energy spectrum of the solar neutrinos, $\frac{d\sigma_e}{dT_e}\left(\frac{d\sigma_{\mu,\tau}}{dT_e}\right)$ is the differential scattering cross section as a function of electron kinetic energy for ν_e ($\nu_{\mu,\tau}$), and P_{ee} is the ν_e

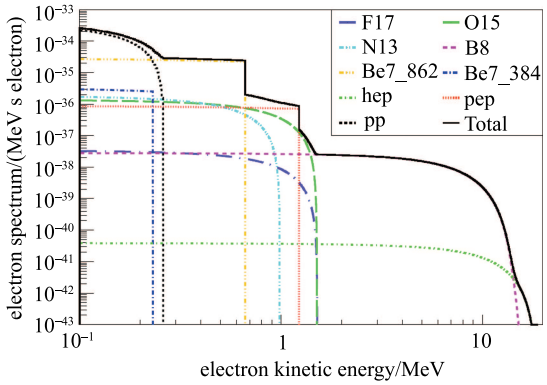

Fig. 9. (color online) Kinetic energy distribution of recoil electrons for each solar neutrino component, in which the MSW oscillation and the high metallicity hypotheses are both considered.

Table 3. Expected electron event rates for different thresholds and metallicity hypotheses. The uncertainties are all from the solar model prediction only.

electron event rate /day/100 ton	>0 keV (GS98) high metallicity	>0 keV (AGS09) low metallicity	>200 keV (GS98) high metallicity	>200 keV (AGS09) low metallicity
pp	132.59 ± 0.80	133.70 ± 0.80	4.557 ± 0.027	4.595 ± 0.028
^{7}Be (0.38 MeV)	1.93 ± 0.13	1.76 ± 0.12	0.228 ± 0.016	0.208 ± 0.015
^{7}Be (0.86 MeV)	46.9 ± 3.3	42.8 ± 3.0	31.6 ± 2.2	28.8 ± 2.0
pep	2.735 ± 0.033	2.792 ± 0.034	2.244 ± 0.027	2.291 ± 0.028
^{13}N	2.45 ± 0.34	1.80 ± 0.25	1.48 ± 0.21	1.09 ± 0.15
^{15}O	2.78 ± 0.42	1.95 ± 0.29	2.03 ± 0.31	1.42 ± 0.21
^{17}F	0.069 ± 0.012	0.0426 ± 0.0072	0.0506 ± 0.0086	0.0312 ± 0.0053
^{8}B	0.443 ± 0.062	0.364 ± 0.051	0.427 ± 0.060	0.351 ± 0.049
hep	0.0009 ± 0.0003	0.0009 ± 0.0003	0.0009 ± 0.0003	0.0009 ± 0.0003

survival probability. The recoiling electron spectra of the solar neutrinos for all the fusion processes can be seen in Fig. 9. The number of electron candidates for the high and low metallicity hypotheses and the effective number of electron candidates with a 200 keV energy threshold are shown in Table 3, where the number of electrons per 100 tons was assumed to be 3.307×10^{31} [43].

3.2.5 Fiducial target mass

In our sensitivity study the fiducial target masses are set to be 1000, 2000, and 4000 tons, respectively.

3.2.6 Detector response model

Three types of target materials were studied for the detection of the recoiling electrons through elastic neutrino-electron scattering.

Liquid scintillator, with its high light yield and low detecting threshold, has been successfully applied in many low-energy neutrino experiments. The liquid scintillator detector response can be approximated by a simple characteristic resolution function. The non-uniform and non-linear detector energy responses can both be corrected, so they do not need to be included in this study. The SNO+ experiment inherited the almost doubled photocathode coverage from the SNO experiment [70] compared to Borexino [71], so a doubled light yield was considered possible in this study. Liquid scintillator was used as a reference material for this study.

Water is the second option under our consideration. The technique developed by the Super Kamiokande experiment [72] is very mature, but the light yield is low.

Slow scintillator is the third option, because of the attractive feature that it can separate scintillating and Cherenkov light and provide additional information for energy reconstruction and background suppression.

Three typical energy resolutions were tested in this study and their values in terms of photo-electron/MeV (PE/MeV) and corresponding resolution functions are summarized in Table 4.

Table 4. Three types of light yields and resolution functions for the detector response.

light yield	resolution function $(\sigma_{\rm E}/E)$	material
200 PE/MeV	$1/\sqrt{200E/{\rm MeV}}$	water (SK)
500 PE/MeV	$1/\sqrt{500E/{\rm MeV}}$	LS or Slow-LS
1000 PE/MeV	$1/\sqrt{1000E/{\rm MeV}}$	LS (SNO+)

3.2.7 Background assumption

There are mainly three categories of backgrounds. 1) Cosmic-ray muon induced spallation backgrounds. With the overburden of Jinping, these backgrounds will be a factor of 200 lower than those in Borexino and a factor of 2 lower than SNO. 2) Internal radioactive beta or gamma backgrounds. They are the residual background remaining in the detecting material regardless of the depth. We assume that these backgrounds can be reduced by purification down to the same level as Borexino. 3) Environment radioactive background. This presents as external gammas for a central detector volume. Borexino background rates were applied in our study, and were scaled according to the surface area.

For simplicity, no quenching effect was considered in the following study, so that for sequential beta and gamma decays, all the gamma energies and beta kinetic energies were added linearly without considering the decay structure of excited states. For the positrons from the beta+ decays, twice the electron mass was added to the detected energy for the positron annihilation.

The external gamma background was modeled by an exponential distribution, motivated by Ref. [43]. The major external ^{208}Tl is assumed to have an exponential energy tail with a decay constant of 0.4 MeV, which is related to the gamma ray attenuation length and fiducial volume buffer dimension.

A summary of the event rates for all the backgrounds can be found in Table 5. Details are given below.

The Borexino-I ^{7}Be refers to the analysis result of

the phase-I ^{7}Be measurement at Borexino [43, 73, 74], from which the fiducial volume mass, live time, and background rates of ^{14}C, ^{85}Kr, ^{210}Bi, and ^{11}C were extracted. The values for ^{14}C and ^{11}C were used for the Jinping study. Other background values, ^{10}C, ^{208}Tl, ^{11}Be, and Ext-^{208}Tl were extracted in a similar way as discussed below.

The Borexino-I pep refers to the analysis result of the phase-I pep measurement at Borexino [43, 75], where the data of 598.3 live days was scaled down by 48.5% for the final selection efficiency. With the technique of three-fold coincidence (TFC), the background rate of ^{10}C was suppressed. The ^{10}C background rate without the TFC technique was taken as a standard value of the Borexino experiment, and then scaled to Jinping. The most significant and representative external gamma background, Ext-^{208}Tl, as a major background was extracted from this analysis and used for the Jinping study.

Borexino-I ^{8}B is for the phase-I ^{8}B analysis at Borexino [76], where the energy beyond 3 MeV was discussed. The reported rates of the high energy backgrounds ^{208}Tl and ^{11}Be were taken to be the standard values for the Borexino experiment, and used for the Jinping study.

The second phase of the Borexino experiment has a much lower ^{85}Kr and ^{210}Bi background rates [77]. A sample with double the live days of data was assumed, in order to compare the phase one analysis. The measured background rates of ^{85}Kr and ^{210}Bi of the second phase were used for the Jinping study.

For comparison purposes, the background situation of the SNO+ experiment [78] is also listed.

Table 5. A summary of the fiducial mass, live time, and backgrounds for all the known running or planned solar neutrino experiments. See the text in Sec. 3.2.7 for the references and calculation methods for each experiment or analysis. Jinping's fiducial mass and resolution will be scanned in the study.

	mass/ 100 ton	time/ day	resolution/ PE/MeV	^{14}C	^{85}Kr	^{210}Bi	^{11}C	^{10}C	^{208}Tl	^{11}Be	Ext-^{208}Tl
				/counts/day/100 ton							
Borexino-I ^{7}Be	0.7547	740.7	500	3.46×10^{6}	31.2	41.0	28.5	0.62	0.084	0.032	2.52
Borexino-I pep	0.7130	290.2	500	3.46×10^{6}	31.2	41.0	2.48	0.18	0.084	0.032	2.52
Borexino-I ^{8}B	1	345.3	500	3.46×10^{6}	31.2	41.0	28.5	0.62	0.084	0.032	2.52
Borexino-II ^{7}Be	0.7547	1480	500	3.46×10^{6}	1	25.0	28.5	0.62	0.084	0.032	2.52
Borexino-II pep	0.7130	580	500	3.46×10^{6}	1	25.0	2.48	0.18	0.084	0.032	2.52
Borexino-II ^{8}B	1	690	500	3.46×10^{6}	1	25.0	28.5	0.62	0.084	0.032	2.52
SNO+	5	1500	1000	3.46×10^{6}	1	25.0	0.29	0.0062	0.084	0.00032	1.47
Jinping	scan	1500	scan	3.46×10^{6}	1	25.0	0.15	0.0031	0.084	0.00016	1.17

3.2.8 Total spectrum

Simulation samples were constructed with solar signals and backgrounds. They were fitted and analyzed for each physics topic below and the corresponding discovery sensitivities will be reported.

3.3 Systematics of the flux measurement

Two systematic uncertainties were considered for the measurement of the solar neutrino flux. One is the fiducial volume definition, which is only related to the bias of vertex reconstruction rather than the resolution. A 1% systematic uncertainty was assumed for the fiducial volume cut. The other is from the energy response of the detector. With the experience of the Borexino experiment and the recent Daya Bay experiment [79, 80], we believe that the uncertainty from the non-linearity and non-uniformity effect in the energy reconstruction can be controlled down to the level of 1%. With a large data sample expected at Jinping, we assumed there was no fitting procedure error as introduced by Borexino analysis. In total, 1.5% systematic uncertainty is assigned to all the flux measurements.

3.4 Precision for each component measurement

Simulations with the inputs from Table 3 and various target masses and energy resolutions were done to evaluate the expected precisions. A fitting example is shown in Fig. 10. The 0.38 MeV to 0.86 MeV ratio

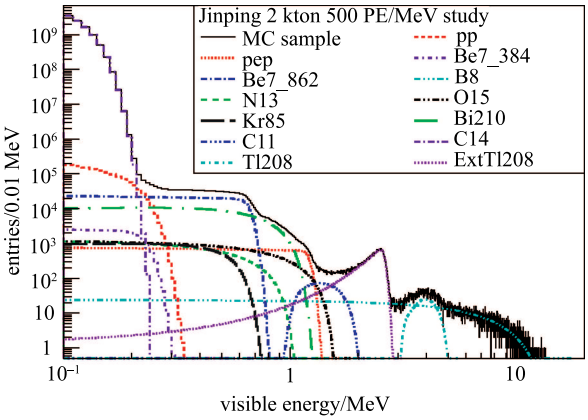

Fig. 10. (color online) Fit results for the simulation sample with a 2000-ton target mass and 500 PE/MeV energy resolution.

of the ^{7}Be lines was fixed according to Table 2. Since the characteristic line shapes for the ^{15}O and ^{17}F were not distinguishable, only the ^{15}O component was considered in the fitter. The hep neutrino contribution was not significant in the fit, and was ignored. Table 6 lists the relative statistical precisions for all the solar neutrino components with the high and low metallicity models.

Table 6. Relative statistical precision of solar neutrino fluxes for three different target masses and energy resolutions. The default results are for the high metallicity assumption and the ones in the parentheses are for low metallicity if significantly different. NA is marked when the relative uncertainty is greater than 50%.

		energy resolution/PE/MeV		
		200	500	1000
fiducial mass 1000 ton	pp	0.02	0.007	0.005
	^{7}Be	0.007	0.006	0.005
	pep	0.07	0.05	0.04
	^{13}N	NA	0.5 (NA)	0.3 (0.4)
	^{15}O	0.3	0.2 (0.4)	0.1 (0.2)
	^{8}B	0.02	0.02	0.02
fiducial mass 2000 ton	pp	0.01	0.005	0.004
	^{7}Be	0.005	0.004	0.004
	pep	0.06	0.03	0.03
	^{13}N	0.4	0.3	0.2 (0.3)
	^{15}O	0.2	0.1	0.08 (0.1)
	^{8}B	0.02	0.02	0.02
fiducial mass 4000 ton	pp	0.01	0.004	0.003
	^{7}Be	0.004	0.003	0.003
	pep	0.04	0.03	0.02
	^{13}N	0.3	0.2 (0.3)	0.2 (0.3)
	^{15}O	0.1 (0.2)	0.07 (0.1)	0.06 (0.09)
	^{8}B	0.01	0.01	0.01

3.4.1 Improvement on the known neutrino components

pp **neutrino:** As shown in Fig. 10, the electron energy from the elastic pp neutrino scattering is slightly higher than that from the main background ^{14}C, and the best signal region for detecting the pp neutrinos is around 0.2–0.3 MeV. The statistical uncertainty on the pp neutrino flux is very sensitive to the energy resolution of the detector, which can reach 1% with the 500 PE/MeV light yield. The total uncertainty will be dominated by the systematic uncertainty. We hope to control the dominant systematic uncertainty and reduce the total uncertainty down below 1%, and this will help to explore the expected difference between the neutrino luminosity and the optical luminosity.

^{7}**Be neutrino:** The ^{7}Be and ^{8}B neutrinos are critical to distinguish the high and low metallicity hypotheses. The ^{7}Be neutrino flux can be measured statistically to better than 1%, which is less dependent on the energy resolution due to the characteristic sharp turn. The total flux uncertainty is dominated by the systematic uncertainty.

^{8}**B neutrino:** The ^{8}B neutrinos suffer the largest matter effect, which makes them sensitive to the vaccum-matter transition phase and the day-night flux asymmetry. The relatively high energy of ^{8}B neutrinos makes them less contaminated by other backgrounds, and because of the broad energy spectrum, the study of ^{8}B neutrinos does not rely on the energy resolution much. The statistical precision of the flux of ^{8}Be neutrinos is expected to be about 1%–2% , which is limited by the target mass, and is comparable to the systematic uncertainty.

pep **neutrino:** The distinguishable structure of the pep neutrino spectrum, like the ^{7}Be neutrinos, makes them easily identifiable. With the three energy resolution options considered, the sensitivities can all reach 7% and even 3% if the target mass can be increased to 2000 tons. The pep neutrinos are one of the key ingredients in the study of the solar model and the vacuum-matter oscillation transition.

3.4.2 Discovery of the CNO neutrinos

CNO neutrino: The flux of CNO neutrinos strongly depends on the metallicity hypotheses and itself is a very interesting subject since the CNO neutrinos are from the main fueling process of high temperature stars, while the pp process is dominant in the Sun because of the relatively low temperature. The major backgrounds for the ^{13}N and ^{15}O neutrino detection are the ^{7}Be and pep neutrinos, and ^{85}Kr and ^{210}Bi decays. An effective identification of the other neutrinos and backgrounds will help to resolve the CNO neutrinos, and this relies on the energy resolution. With a resolution of 500 PE/MeV or better, discovery of the ^{15}O neutrinos at Jinping will be possible (the relative error is better than 30%) for the high metallicity assumption. With a larger target mass, for example 2000 tons, the discovery potential will be significant for both high and low metallicity assumptions.

3.5 Matter-vacuum transition phase

The transition of oscillation probability from the matter-governed region to the pure vacuum-like region is a very interesting phenomenon of the MSW effect. This effect has been studied by Borexino [43, 76], Super Kamiokande [72], SNO [78], and previous experiments. Experimentally, however, the oscillation in the transition region is still loosely constrained, giving chances for non-standard effects enhanced by an MSW-like resonance, for example as described in Refs. [53, 81–84]. The current status is shown in Fig. 11. With the Jinping

simulation, the expected flux measurements are compared with the predictions with neutrino energy and recoil electron kinetic energy, which are shown in Fig. 11 and 12, respectively. For Fig. 12, the uncertainty of each bin is assigned as the square root of the full statistics of each bin including all the backgrounds and signals, and, for a better demonstration, the bin ranges were adjusted according to the statistics of each individual signal region.

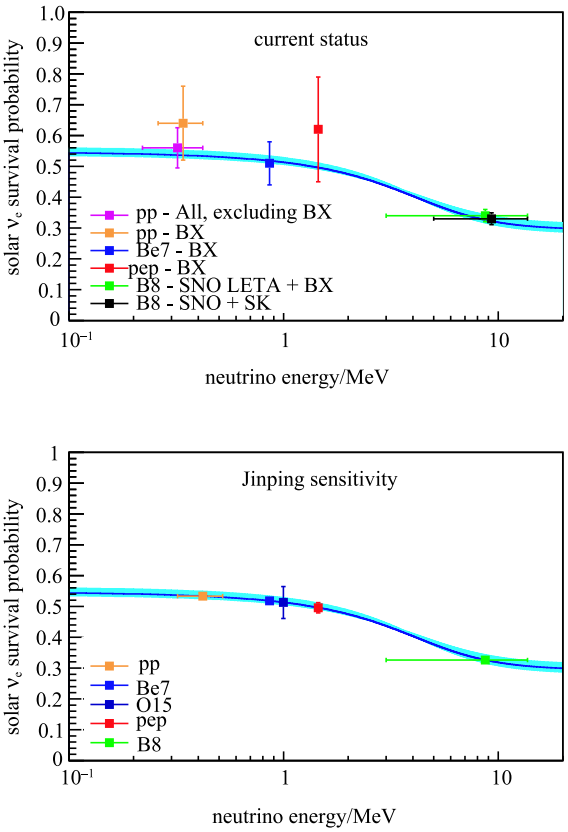

Fig. 11. (color online) The transition of oscillation probability from the vacuum to matter effect as a function of neutrino energy. The central line is for the theoretical prediction, while the shaded area is obtained by marginalizing θ_{12}, θ_{13}, and Δm^2_{12} with the present experimental uncertainty. Top plot: Data points plotted are the present measurements [74, 75, 77]. Bottom plot: We assume a 2000-ton target mass, 1500-day exposure, a resolution of 500 PE/MeV, and the low metallicity hypothesis. The five points with error bars are the simulation results for pp, ^{7}Be, pep, ^{15}O and ^{8}B, in which the central values are set to the true ones, the y-error bars include both statistical and systematic uncertainties and the x-error bars correspond to the range of energy measurement, while the ^{15}O x-error is omitted for a clear view.

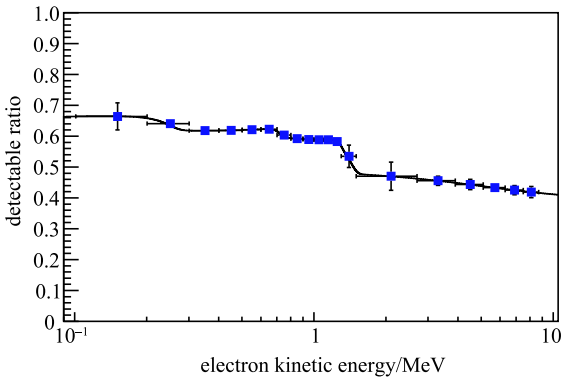

Fig. 12. (color online) The ratio of the detected kinetic energy spectrum of recoil electrons after background subtraction over the non-oscillation truth. Here we assumed a 2000-ton target mass, 1500-day exposure, a resolution of 500 PE/MeV, and the low metallicity hypothesis. The solid line is for the theoretical prediction and the points are simulated data with statistical errors. Because of the large correlation among the points, the systematic uncertainties are not included.

3.6 Day-night asymmetry

After solar neutrinos pass through the Earth, electron neutrinos may be regenerated because of the MSW matter effect [57], which leads to a slightly higher survival probability during the night than during the day time. The average survival probability is very sensitive to Δm^2_{21} and the density profile at the nearby surface of the Earth [58, 59]. The latter can cause a day-night asymmetry varying around 1%–3% for the rate of solar neutrinos. With 5 years of data-taking and a 2000-ton detector, the total statistics of ^{8}B could reach 10000 events, which is insufficient to have a conclusive measurement of the day-night asymmetry.

3.7 Metallicity problem

With the expected improvements in the measurement of solar neutrino fluxes, we have carried out a study of the hypothesis test for the solar models with the high and low metallicities. The study is focused on the experimental capability with given oscillation parameters, because the theoretical uncertainties of the solar neutrino flux predictions are difficult to quantify currently [23]. The evaluation was done assuming 2000-ton target mass and 1500-day exposure.

The ability to distinguish two hypotheses, separation S, is defined as

$$S = \left[\sum_{i,j}(F_{h,i}-F_{l,i})(V^{-1})_{ij}(F_{h,j}-F_{l,j})\right]^{1/2}, \qquad (10)$$

where $F_{h,i}$ and $F_{l,i}$ are the predicted neutrino fluxes for the i-th component with the high (h) and low (l)

metallicities, respectively, and V is the covariance matrix, which follows the usual definition as

$$V_{ij} = \sigma_i \sigma_j \rho_{ij}, \tag{11}$$

where σ_i is the uncertainty of the i-th component and ρ_{ij} gives the correlation between the i-th and j-th components.

Firstly, an optimistic calculation of the separation, $S_{\rm opt}$, between the two hypotheses was done assuming all of the flux measurements were independent. By simplifying Eq. (10),

$$S_{\rm opt} = \left[\sum_i S^2_{{\rm opt},i}\right]^{1/2} = \left[\sum_i (F_{h,i} - F_{l,i})^2/\sigma_i^2\right]^{1/2}, \tag{12}$$

where $S_{{\rm opt},i}$ gives the separation achieved for the i-th component. Table 7 gives the inputs for calculating $S_{\rm opt}$, including the flux difference between the two hypotheses, the expected experimental uncertainties, $\sigma_{{\rm exp},i}$, $S_{{\rm opt},i}$, and the theoretical uncertainties $\sigma_{{\rm theory},i}$. The final result is

$$S_{\rm opt} = 9.6, \tag{13}$$

which can be treated as a 9.6 σ rejection to the high metallicity hypothesis and vice versa. The most powerful separations are expected from the ^{7}Be, ^{15}O, and ^{8}B neutrinos.

Table 7. Details of the high and low metallicity hypotheses test. The second column shows the flux difference, i.e. GS98-AGS09 [50, 60]. The third column gives the expected absolute experimental error, $\sigma_{{\rm exp},i}$, which is calculated according to the GS98 flux estimation and the expected statistical and systematic errors. The fourth column is the separation for the i-th component, $|S_{{\rm opt},i}|$, as defined in Eq. 12. In the last column, the absolute theoretical uncertainty for the i-th component, $\sigma_{{\rm theory},i}$, is presented for comparison. The flux difference, $\sigma_{{\rm exp},i}$, and $\sigma_{{\rm theory},i}$ are in units of 10^{10} (pp), 10^9 (^{7}Be), 10^8 (pep, ^{13}N, ^{15}O), 10^6 (^{8}B, ^{17}F), and 10^3 (hep) cm^{-2}s^{-1}.

	$F_{h,i} - F_{l,i}$	$\sigma_{{\rm exp},i}$	$\lvert S_{{\rm opt},i}\rvert$	$\sigma_{{\rm theory},i}$
pp	0.05	0.10	0.53	0.036
^{7}Be	−0.44	0.078	5.7	0.32
pep	0.03	0.048	0.62	0.018
^{13}N	−0.79	0.89	0.89	0.30
^{15}O	−0.67	0.23	3.0	0.28
^{17}F	−2.12	-	-	0.76
^{8}B	−0.99	0.14	7.1	0.64
hep	0.27	-	-	2.49

Secondly, a model separation quantity $S_{\rm cons}$ was conservatively evaluated taking into account the contribution from the ^{7}Be, ^{8}B, and ^{15}O neutrinos, and the experimental correlations among them. The correlations stem from the fitting procedure to separate the ^{7}Be and ^{8}B components, since the statistical precisions are relatively high, as listed in Table 6. The major sources of systematic errors, target mass and energy response, might be fully correlated among all the neutrino components for the worst case. It should be noted that the relative systematic uncertainty of 1.5% is dominant for the ^{7}Be neutrinos and significant for the ^{8}B neutrinos. As a result, the correlation between them is as high as 50%, degrading the power to distinguish the models. The correlation matrix between them is given below

$$\rho = \begin{bmatrix} 1 & 0.1581 & 0.5799 \\ 0.1581 & 1 & 0.1104 \\ 0.5799 & 0.1104 & 1 \end{bmatrix}, \tag{14}$$

where the rows and columns are arranged sequentially for the ^{7}Be, ^{15}O, and ^{8}B, respectively. The calculation gives

$$S_{\rm cons} = 7.6. \tag{15}$$

As a conclusion, the proposed Jinping neutrino experiment has the capability to resolve the high and low metallicity hypotheses in the given references with 7–10 σ with the fixed input of present mixing angles. We expect the uncertainties on these mixing angles will be improved with terrestrial experiments.

3.8 Conclusion and summary

Based on the discussion in this section, with 2000-ton fiducial mass and 500 PE/MeV light yield, the expected outcome for the proposed Jinping neutrino experiment running over 5 years is very promising to make a discovery of the CNO neutrinos and to significantly improve the measurements of the pp, ^{7}Be, and pep neutrino fluxes. The experiment can also provide a stronger constraint on the vacuum-matter transition to the MSW effect, and have the experimental capability to distinguish the high and low metallicity hypotheses in the given references. Due to the limited target mass, physics relying on the statistics of ^{8}B neutrinos cannot be precisely probed, for example, the day-night asymmetry. In this study, we did not discuss the possible improvement of the measurement of neutrino mixing angles and the possibility to rule out other new physics.

4 Geo-neutrinos

4.1 Introduction

Identifying and understanding the Earth's energy budget is a fundamental question in geology, as it defines the power that drives plate tectonics, mantle convection, and the geodynamo [85]. The motivation for understanding geo-neutrinos starts with the wish to understand our planet.

The Earth's total heat flow is currently estimated to be 46 ± 3 TW [86]. The driving power comes presumably from two sources: 1) the heat evolved from decay of radiogenic isotopes, and 2) primordial energy that resulted from the accretion of the planet and the gravitational differentiation of iron sinking to the center of the Earth [87, 88]. Estimates for the radiogenic heat production (from K, Th and U, >99%) in the Earth cover a continuum of compositional models that can be defined by three groups: (1) low Q models (10–15 TW of power), medium Q models (17–22 TW) and high Q models (>25 TW), which were previously classified as cosmochemical, geochemical, and geodynamical models, respectively [87]. The continents are estimated to accounts for 7 TW of the total budget of heat-producing elements, which translates to the mantle having insignificant (3 TW) to substantial (>18 TW) amounts of radiogenic power [89].

Geo-neutrinos are produced by radioactive decays from inside the Earth, with only those from the ^{232}Th and ^{238}U decay chains being detectable because their energies are >1.8 MeV, the threshold for initiation of inverse beta decay (IBD). Quantifying the flux of these geo-neutrinos will place limits on the radiogenic power in the planet and provide authoritative insights into the building blocks of the Earth and the energy driving plate tectonics. The field of neutrino geophysics only became practical recently by the advent of large underground neutrino detectors, i.e. the KamLAND [90–92] and Borexino [93–95] experiments.

The current experimental status can be seen in Ref. [88]. The fuel that drives the Earth's engine comes from unknown proportions of primordial energy from assembling the planet and nuclear energy from the heat produced during natural radioactive decay. There is an order of magnitude uncertainty in present-day estimates of the amount of radiogenic power driving mantle dynamics. The existing measurements of the Earth's flux of geoneutrinos [90–95] reveal the amount of uranium and thorium in the Earth, and have excluded a fully radiogenic Earth, but regrettably, because of the considerable uncertainty from these models, cannot discriminate between the three competing compositional models for the Earth. The most recent result from the Borexino experiment [95] reported a figure for the mantle flux of geo-neutrinos, although with about 75% uncertainty at the 1-sigma level.

The mantle neutrinos are of the most theoretical interest, but the corresponding fraction is only from 15% to 30% for any given continental experiments [96], and the distribution of heat producing elements is not precisely known. The crustal geo-neutrino flux is the best known of the contributors to the total flux, as it the most accessible part of the Earth. Calculating the geo-neutrino contribution from the continental crust is done by integrating data from geophysical [97–99] and geochemical [96] surveys of continents, with detailed regional studies for the first 500 km surrounding the detector [100] as this region typically contributes half of the total geo-neutrino signal. Critical constraints on the Earth models will come from precise measurements of the Earth's geo-neutrino flux.

A natural nuclear fission reactor at the center of the earth with an estimated power output of 3–10 TW has been proposed as the energy source of the earth's magnetic field [101]. Experimental results may critically assess such assumptions and set limits on its presumed power contribution.

Due to its location far away from nuclear power plants, Jinping is an ideal site to precisely measure the geo-neutrino flux and to probe for potential geo-reactors. Next we will introduce geo-neutrino signals in Section 4.2, the critical backgrounds from reactor neutrinos and other contributors in Section 4.3, and the sensitivity to study geo-neutrinos at Jinping in Section 4.5. The sensitivity for geo-reactors will be briefly discussed in Section 4.6.

4.2 Geo-neutrino signal

This section discusses the spectrum and flux of the geo-neutrinos, together with their detection.

4.2.1 Geo-neutrino spectrum and flux

Natural decays from the ^{238}U and ^{232}Th families and ^{40}K produce heat:

$$\begin{aligned}
&{}^{238}_{92}\mathrm{U} \to {}^{206}_{82}\mathrm{Pb} + 8\alpha + 6\beta^- + 6\bar{\nu}_\mathrm{e} + 51.698\ \mathrm{MeV},\\
&{}^{232}_{90}\mathrm{Th} \to {}^{208}_{82}\mathrm{Pb} + 6\alpha + 4\beta^- + 4\bar{\nu}_\mathrm{e} + 42.652\ \mathrm{MeV},\\
&{}^{40}_{19}\mathrm{K} \to {}^{40}_{20}\mathrm{Ca} + \beta^- + \bar{\nu}_\mathrm{e} + 1.311\ \mathrm{MeV} \quad (\mathrm{BR} = 89.3\%),\\
&{}^{40}_{19}\mathrm{K} + \beta^- \to {}^{40}_{18}\mathrm{Ar} + \nu_\mathrm{e} + 1.505\ \mathrm{MeV} \quad (\mathrm{BR} = 10.7\%).
\end{aligned} \tag{16}$$

The predicted beta-decay spectra of the antineutrinos are from Ref. [102].

The geo-neutrino flux prediction depends on the geo-models and locations. The recent flux prediction at the Jinping site in Ref. [89] was used for the sensitivity study in this section. The total neutrino flux is $58.5^{+7.4}_{-7.2}$ TNU including both U and Th.

4.2.2 Geo-neutrino detection

In principle, neutrinos can be detected via either the elastic scattering process or the inverse beat decay (IBD) reaction. Owing to the low cross-section and the potential solar neutrino background, we do not expect the first process can be used at Jinping. The electron antineutrinos will be detected using the IBD reaction chain [103]

$$\bar{\nu}_\mathrm{e} + \mathrm{p} \to \mathrm{e}^+ + \mathrm{n}, \text{ followed by } \mathrm{n} + \mathrm{H} \to \mathrm{d} + \gamma\ (2.2\ \mathrm{MeV}). \tag{17}$$

Depending on the detector type, the energy of electron antineutrinos can be approximately calculated by either $T_{e^+}+1.8$ MeV in water or $T_{e^+}+0.78$ MeV in scintillator. Here, T_{e^+} is the visible energy of the positron, and the tiny energy of neutron recoil is neglected. The 1.0 MeV difference in scintillator is due to the fact that the visible energy of the positron is actually the sum of the positron kinetic energy and the annihilation γ energy. Because of the soft geo-neutrino spectra and the high Cherenkov threshold, the measurement of geo-neutrinos can only be performed in liquid scintillator detectors or water-based scintillator detectors.

4.3 Geo-neutrino backgrounds

4.3.1 Reactor antineutrino background

Reactor electron antineutrinos are an irreducible background to the detection of geo-neutrinos. The only way to reduce the reactor neutrino flux is to apply the $1/r^2$ law and place the detector far away from nuclear power plants. Fortunately, the location of Jinping is at least 1200 km away from any nuclear power plant either operational or under construction, and is therefore the best site for geo-neutrino experiments of all the existing experiments. Below, we evaluate the reactor antineutrino background at Jinping.

4.3.2 Differential neutrino flux of a single reactor

Reactor antineutrinos are primarily from the beta decays of four main fissile nuclei ^{235}U, ^{238}U, ^{239}Pu, and ^{241}Pu. The differential $\bar{\nu}_e$ flux, $\phi(E_\nu)$, for a reactor is calculated by [104]

$$\phi(E_\nu)=\frac{W_{\rm th}}{\sum_i f_i e_i}\sum_i f_i S_i(E_\nu), \quad (18)$$

where i sums over the four isotopes, $W_{\rm th}$ is the thermal power of a reactor which can be found in the IAEA [105, 106], f_i ($\sum_i f_i=1$) is the fission fraction of each isotope, e_i is the average energy released per fission of each isotope, and $S_i(E_\nu)$ is the antineutrino spectrum per fission of each isotope. A set of typical fission fractions, f_i, and the average energy released per fission, e_i, are listed in Table. 8.

Table 8. Fission fraction and average released energy of each isotope [104].

isotope	f_i	e_i/MeV/fission
^{235}U	0.58	202.36 ± 0.26
^{238}U	0.07	205.99 ± 0.52
^{239}Pu	0.30	211.12 ± 0.34
^{241}Pu	0.05	214.26 ± 0.33

4.3.3 Total differential reactor neutrino flux

To get the total reactor neutrino background spectrum at Jinping, $\phi_{\rm Jinping}(E_\nu)$, we used the thermal powers of all the currently running and under construction nuclear power plants from the IAEA [105], and took into account the electron antineutrino survival probability. $\phi_{\rm Jinping}(E_\nu)$ is expressed as

$$\phi_{\rm Jinping}(E_\nu)=\sum_i^{Reactors}\phi_i(E_\nu)P_{\bar{\nu}_e\to\bar{\nu}_e}(E_\nu,L)\frac{1}{4\pi L^2}, \quad (19)$$

with

$$P_{\bar{\nu}_e\to\bar{\nu}_e}(E_\nu,L)\approx 1-\sin^2 2\theta_{12}\sin^2[1.267\frac{\Delta m^2_{21}({\rm eV})L({\rm km})}{E_\nu({\rm GeV})}], \quad (20)$$

where E_ν is the neutrino energy, L is the distance from each reactor to the Jinping site, and θ_{12} and Δm^2_{21} are neutrino oscillation parameters. L is calculated using the longitude and latitude coordinates for each nuclear power plant and Jinping site, and θ_{12} and Δm^2_{21} are set to be 0.586 and 7.58×10^{-5} eV^2, respectively. Table 9 lists the numerical results for the fluxes.

Table 9. Reactor neutrino flux at Jinping.

Jinping	operation		construction		total
	China	others	China	others	
$\phi_\nu/(10^5{\rm cm}^{-2}{\rm s}^{-1})$	3.71	2.73	6.20	0.35	12.99

4.3.4 Other non-$\bar{\nu}_e$ backgrounds

Other possible backgrounds are the cosmic-ray muon induced ^{9}Li and ^{8}He, (α, n) background, and the accidental coincidence background. According to the recent publication by Borexino [95], the signal-to-non-$\bar{\nu}_e$-background ratio is ~100, so these backgrounds were ignored in this study.

4.4 Fiducial mass for geo-neutrinos

The detection of $\bar{\nu}_e$'s is through the IBD process in Eq. (17). Since the delayed-coincidence technique is applied to identify the prompt and delay signal pair, the ratio of signal to background can be significantly improved. Consequently, a lesser requirement on the fiducial volume can be applied, increasing the target mass from 2000 tons to 3000 tons.

4.5 Sensitivity for geo-neutrinos

The event rates of geo-neutrino signal, reactor neutrino background, and the sensitivity of observing geo-neutrinos and determining the Th/U ratio are discussed in this section.

4.5.1 Signal and background rates and spectra

The detectable spectra from the IBD process can be calculated as

$$R_{\rm Jinping}(E_\nu)=\phi_{\rm Jinping}(E_\nu)\times\sigma(E_\nu). \quad (21)$$

With a modest setup, i.e. 1 kiloton fiducial volume and 1500 days' data-taking, the total signal and reactor background rates are summarized in Table 10. Within the

geo-neutrino signal region, <2.8 MeV, the reactor neutrino background rate is less 30/kton/1500 day. The signal to background ratio is rather promising.

Table 10. Total geo-neutrino and reactor neutrino event rates at Jinping.

	geo-neutrinos			reactors
	^{238}U	^{232}Th	Total	
rate/kton/1500 day	138	34	172	64

4.5.2 Sensitivity for geo-neutrino signals

According to the true signal and background spectra, and the exposure of 3 kiloton of target mass, 1500 days of data-taking, and 500 PE/MeV detector energy resolution, we randomly sampled the spectra and performed a likelihood fit with both signals and background. One example fit with Th/U ratio fixed to the known value is given in Fig. 13. The precision of the total geo-neutrino flux can be determined down to 4%. The other fit with the Th and U fractions free is also shown in Fig. 13. The ^{238}U fraction can be determined to 6%, and the ^{232}Th fraction's precision can reach 17%.

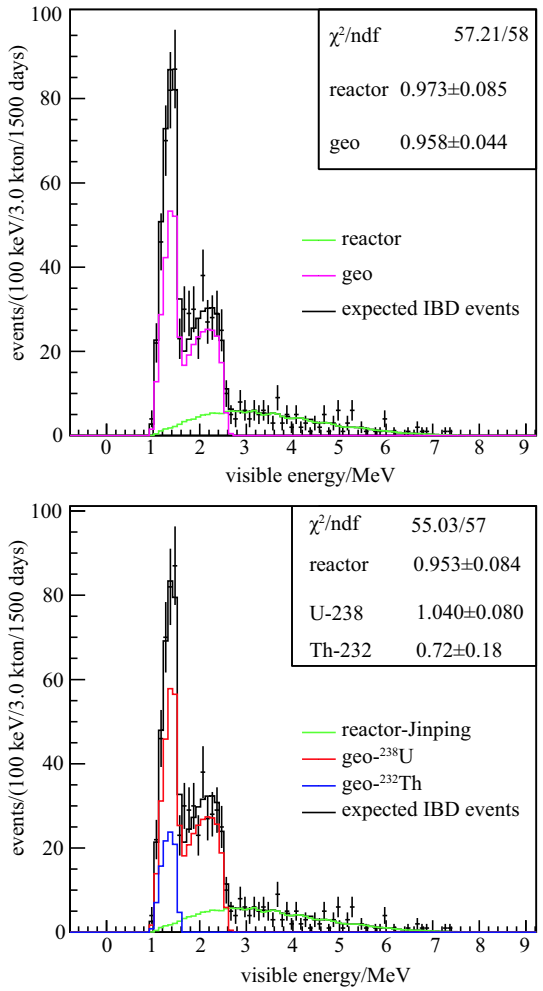

Fig. 13. (color online) Fit result for both the geo-neutrino signals and backgrounds. The top plot is fitted with the Th/U ratio fixed to 3.9, while in the bottom plot Th and U components are fitted separately. Numbers shown in the corner are χ^2/ndf and the ratios of the fit result to the nominal value for the reactor background and geo-neutrinos.

4.5.3 Th/U ratio

With 5000 tests of random sampling and fitting, we estimated the expected precision to determine the ratio of U to Th components, i.e. how well we can determine the expected chondritic mass Th/U ratio of 3.9. The result is that the Th/U ratio can be well measured, with a precision of 27%.

4.5.4 Sensitivity to geo-neutrino models

With the 4% precision in determining the total geo-neutrino flux, the result can be compared with the model predictions. Shown in Fig. 14 are two possible outputs with uncertainties overlaid on the model predictions of geo-neutrino flux as a function of heat production. The prediction has two main uncertainties. The first is a 10% uncertainty of the crust neutrino flux, and the other is the distribution of the mantle neutrinos, which could be uniform in the mantle or in the extreme case only concentrate around the border of the mantle and the core. With the expected improvement of the geo-neutrino flux measurement, it should be possible to accept or reject some geo-neutrino predictions. But, certainly, a more precise geological survey of the near-by crust, and, if possible, a better understanding of the mantle neutrino distribution, are necessary to decrease the prediction uncertainty.

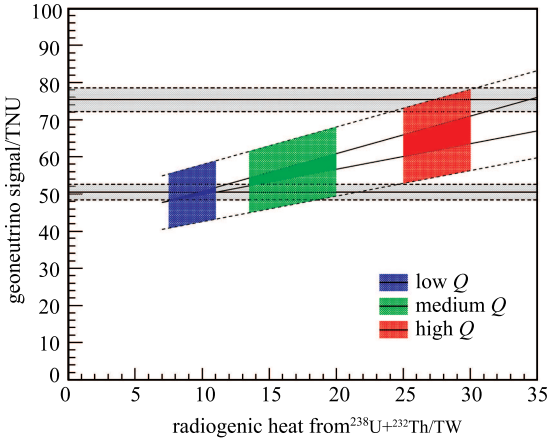

Fig. 14. (color online) The geo-neutrino sensitivity vs geo-neutrino model predictions at Jinping. The three filled regions in the plot delimit, from the left to the right, low- medium- and high-Q models, respectively. The two horizontal bars are plotted at two possible geo-neutrino flux assumptions with Jinping geo-neutrino measurement sensitivity.

4.6 Sensitivity for a geo-reactor in the core

The geo-reactor neutrinos are predicted to have the same energy distribution as man-made reactors. The number of events over 2.9 MeV was counted. According to Poisson statistics, a 95% upper limit was deduced for the total power of the geo-reactor in the Earth core:

$$P_{\rm reacto} < 2.3 \text{ TW (95\% CL)}, \tag{22}$$

which can conclusively confirm or exclude the 3-10 TW geo-reactor proposal.

4.7 Discussion and summary

The reactor neutrino background can be suppressed significantly, given the ideal location of the Jinping detector. As discussed in Section 4.5, the expected total number of geo-neutrino candidates can be over 500 for a 3 kiloton target mass with 1500-liveday exposure, while the number of background events from nuclear power plants is evaluated to be less than 100 below 2.8 MeV. The flux of geo-neutrinos can be determined with a precision of 4% and the ratio of Th/U can be determined to better than 27%. As shown in Section 4.6, a conclusive confirmation or rejection of a geo-reactor with 3–10 TW can also be made.

5 Supernova burst neutrinos

5.1 Introduction

On 1987 February 23, about two dozen supernova (SN) burst neutrinos were observed in the Kamiokande II, IMB, and Baksan experiments from the stellar collapse SN 1987A, resulting from the star Sanduleak -69202 exploding in the Large Magellanic Cloud, about 50 kpc away from the Earth [107–112]. This was the first observation of a supernova neutrino burst and SN 1987A remains the only known low-energy astrophysical neutrino source since then except for the Sun. SN burst neutrinos carry away almost all of the gravitational binding energy of a stellar collapse, and are important in studying the core-collapse supernova (ccSN) mechanism [113]. SN neutrinos can also provide a large range of physical limits on neutrino properties [114–116]. Since ccSN explosions are likely the strongest galactic sources of gravitational waves, joint observations of both SN burst neutrinos and gravitational waves could provide deep insight into ccSN explosions as well as other fundamental physics [117].

The detection of SN burst neutrinos is so important, but galactic SN explosions occur with a rate of only a few per century [118], which makes the detection a once-in-a-lifetime opportunity. SN neutrinos are expected to arrive at the Earth a few hours before the visual SN explosion, which enables a precious early warning for a SN observation [113]. The Supernova Early Warning System (SNEWS) [119, 120] collaborates with experiments sensitive to ccSN neutrinos, to provide the astronomy community with a very high-confidence early warning of a SN occurrence, allowing them to point more powerful telescopes or facilities at the event [121].

5.2 Supernova burst neutrino signal

We studied the 1987A-type ccSN model, in which the SN burst neutrinos have three main phases, including prompt $\nu_{\rm e}$ burst, accretion, and cooling, respectively [113]. The duration of 10 seconds covers 99% of the luminosity carried off by all flavors of neutrinos and antineutrinos in a SN explosion. The energy spectrum of SN burst neutrinos follows a quasithermal distribution [122],

$$f_\nu(E) \propto E^\alpha {\rm e}^{-(\alpha+1)E/E_{\rm av}}, \tag{23}$$

where $E_{\rm av}$ is the average energy and α describes the amount of spectral pinching. In this study, $E_{\rm av}$ is set to be 12.28 MeV and α to be 2.61, which correspond to the cooling phase for SN burst $\bar{\nu}_{\rm e}$'s, and we chose a 10-second search window for SN burst neutrinos.

The SN burst neutrinos are emitted in the few-tens-of-MeV range, and the detected neutrinos are dominated by IBD events [123] in a liquid scintillator detector with a fraction of about 90%. The coincidence of IBD prompt signal from the positron (a 0.78-MeV downward shift of neutrino energy in general, see Section 4.2.2) with the delayed gamma emission (∼2.2 MeV) of the IBD neutron capture on H provides a clear $\bar{\nu}_{\rm e}$ signature against the uncorrelated backgrounds. Based on the chemical decomposition, the IBD cross section, and SN burst neutrino flux [113], the expected number of SN burst neutrinos can be determined by

$$N = N_0 \times \frac{L_{\bar{\nu}_{\rm e}}}{5\times10^{52}{\rm erg}} \times \left(\frac{10\,{\rm kpc}}{D}\right)^2 \times \left(\frac{TM}{1\,{\rm kt}}\right), \tag{24}$$

where N_0 corresponds to the expected number (∼300) of SN burst neutrinos at a distance (D) of 10 kpc and a target mass (TM) of 1 kiloton. Generally, the luminosity (L) emitted is fixed for the study, which may vary with models. No selection efficiency is involved here.

Note that the total neutrino flux could be measured by using elastic neutrino - proton scattering as proposed in Refs. [124, 125]. For that, the quenching of protons in LAB has to be known [126], which was measured recently. Hence a new opportunity could also be explored.

5.3 Supernova trigger sensitivity

A supernova trigger system can be implemented with one or several detectors. This system relies on an online scan for any increase of IBD signals within a sliding 10-second window as detailed in Ref. [127]. The Jinping experiment is also aiming to be part of SNEWS in the future.

For the IBD selection in a liquid scintillator detector at Jinping, a prompt signal energy cut, 10–50 MeV, a 3σ delayed energy cut for the 2.2 MeV gamma peak from neutron capture on hydrogen, and a 1–1000 μs prompt-delayed time interval cut are needed. The total selection efficiency is estimated to be ∼85% based on the SN burst neutrino energy spectrum resulting from Eq. (23) and the nH analysis of the measurement of θ_{13} at Daya Bay [128, 129]. This selection efficiency will be used to calculate the detection probability of the supernova trigger, which is defined as the probability that a supernova neutrino burst will be detected.

Requiring $\geqslant$2 IBD candidates in a 10-second window will suppress the background to a negligible level, due to the quite low cosmogenic background rate at Jinping. The detection probability of a supernova trigger is shown in Fig. 15 as a function of distance to the Earth.

Notice that the most distant edge of the Milky Way is just 23.5 kpc from the Earth and SN 1987A exploded at a distance of 50 kpc. The larger distance will cover more SNs.

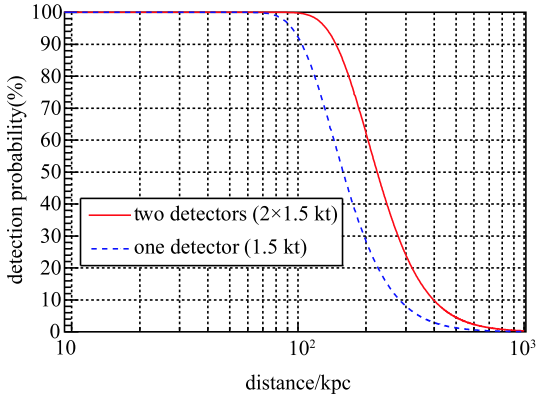

Fig. 15. (color online) Supernova detection probability.

5.4 Discussion

The detection probability of a supernova trigger at Jinping is expected to be 100% throughout a 100 kpc distance in the scenario of two detectors with 1500 fiducial target mass each. This sensitivity is comparable to the Super-Kamiokande experiment [130].

The 10 MeV threshold can be even lower due to the low background rate, increasing the selection efficiency of SN burst neutrinos and covering more SN models with soft neutrino energy spectra.

With the slow liquid scintillator, the pointing ability of the SN neutrino bursts could be achieved by reconstructing the direction of Cherenkov light [131] from the neutrino-electron scattering interactions as Super-Kamiokande does.

6 Supernova relic neutrinos

Supernova relic neutrinos (SRNs), also known as the Diffuse Supernova Neutrino Background (DSNB), is highly interesting for neutrino astronomy and neutrino physics. As described in the previous section, the chance to detect supernova burst neutrinos is rather rare. However neutrinos emitted from past core-collapse supernovae have accumulated and formed a continuum diffuse background, so the chance to discover supernova relic neutrinos is relatively higher. Observation of supernova relic neutrinos will reveal the process of stellar evolution and the history of our universe, and it is a unique tool for astronomy research. Experimental searches have been carried out by Super Kamiokande [132–134], KamLAND [135], Borexino [136], and SNO [137]. However, no SRN signal has been found yet. In this section, we will estimate the future prospects of the Jinping underground experiment.

6.1 SRN models

The SRN spectrum can be predicted by [138]:

$$\frac{\mathrm{d}\phi}{\mathrm{d}E_\nu}(E_\nu)=\int_0^\infty [(1+z)\varphi[E_\nu(1+z)]][R_{\rm SN}(z)]\left[\left|\frac{c\,\mathrm{d}t}{\mathrm{d}z}\mathrm{d}z\right|\right], \tag{25}$$

where the first term within the integral is an average supernova neutrino spectrum $\varphi[E_\nu]$ and then appropriately redshifted, the second term, $R_{\rm SN}(z)$, is a core-collapse rate density as a function of redshift z, and the last term is the known cosmological line-of-sight factor.

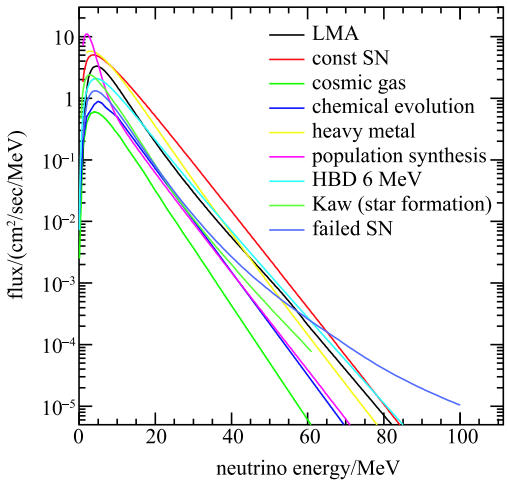

Fig. 16. (color online) Model dependence of $\bar{\nu}_e$ energy spectra for supernova relic neutrinos.

Many models have been proposed to predict the SRN flux and spectrum. In this analysis we will compare the following model predictions with the sensitivity of Jinping: LMA [139], constant SN [140], cosmic gas [141],

chemical evolution [142], heavy metal [143, 144], population synthesis [145], HBD 6 MeV [146], star formation rate [147], and failed SN [148]. The most interesting $\bar{\nu}_e$ energy spectra from the above models are shown in Fig. 16. The average energy of supernova relic neutrinos is highly red-shifted from 20 MeV to below 5 MeV for all models, and the total flux predictions among the models are within about an order of magnitude.

6.2 Detection of SRNs

There are three flavors of neutrinos and anti-neutrinos in SRN, among which $\bar{\nu}_e$'s are most likely to be detected because of the large cross section of IBD in hydrogen (free proton) rich material within the energy region of several tens of MeV and the powerful rejection with delayed coincidence with neutron capture.

Liquid scintillator and slow liquid scintillator were studied as the detecting material, since both have a high efficiency for tagging the delayed neutron to reject accidental backgrounds [134–136]. The gadolinium-loaded water technique [149] was skipped in this study.

In liquid scintillator detectors, the high $\mathrm{d}E/\mathrm{d}x$ deposited by protons and alphas makes it possible to be differentiated from beta and gamma by a pulse shape analysis [150].

In slow scintillator, low energy protons, alphas, and muons in the interesting energy region cannot produce Cherenkov light in the search for SRNs. If the slow scintillator can be used to distinguish Cherenkov and scintillation light, it will be a more powerful tool to suppress backgrounds.

The SRN event rate to be detected via the IBD process can be calculated by

$$\frac{\mathrm{d}R}{\mathrm{d}E_\nu} = \frac{\mathrm{d}\phi}{\mathrm{d}E_\nu} \times \sigma(E_\nu) \times N_\mathrm{p} \times T, \tag{26}$$

where $\sigma(E_\nu)$ represents the differential IBD cross section [103], N_p is the number of free protons in the target, and T is the data-taking time. The target mass for the IBD signal will be about 3 kilotons. The differential detectable or visible energy, E_vis, spectra per kiloton detector per year is shown in Fig. 17, and the expected event rates in the most interesting region of 10–30 MeV are listed in Table 11.

6.3 Backgrounds

There are six main types of backgrounds for the SRN detection: 1) accidental coincidences; 2) reactor $\bar{\nu}_e$'s; 3) fast neutrons induced by energetic cosmic-ray muons; 4) ^{9}Li or ^{8}He radioactive isotopes induced by energetic cosmic-ray muons; 5) atmospheric neutrino background through a charge current (CC) process; and 6) atmospheric neutrino background through a neutral current (NC) process. The estimation of the background rates is explained below.

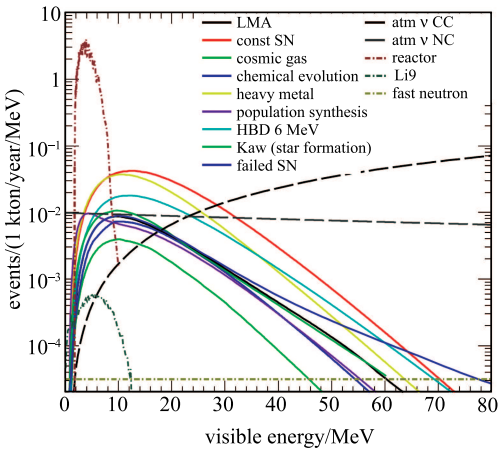

Fig. 17. (color online) Visible energy spectra of supernova relic neutrinos for different models and visible energy spectra of all the possible backgrounds.

Table 11. Expected event rates for the supernova relic neutrinos and the corresponding backgrounds with E_vis in the range around 10–30 MeV. For the signal, the ranges of several models' predictions are printed. Background rates are calculated assuming a liquid scintillator target, and the atmospheric CC and NC background rates in parentheses are the results with a slow liquid scintillator target.

event rate	$\frac{1}{\text{kton-year}}$	$\frac{1}{10\ \text{kton-year}}$	$\frac{1}{20\ \text{kton-year}}$
signal	0.05–0.66	0.5–6.6	1–13
accidental	0	0	0
reactor	0	0	0
fast neutron	0.7×10^{-3}	7×10^{-3}	14×10^{-3}
^{9}Li/^{8}He	1×10^{-3}	10×10^{-3}	20×10^{-3}
atmos. CC	0.2 (0.1)	2 (1)	4 (2)
atmos. NC	0.2 (0.1)	2 (1)	4 (2)
total bkg.	0.4 (0.2)	4 (2)	8 (4)

6.3.1 Accidental coincidence

Accidental coincidence background was considered to be negligible given the ideal location, cleanness of the neutrino detector and concrete estimation [151].

6.3.2 Reactor $\bar{\nu}_e$

Reactor $\bar{\nu}_e$ events are identical to the SRN signal except for the energy spectrum, which is below 10 MeV as shown in Fig. 17. A requirement on energy above 10 MeV together with the fact that there is no nuclear power plant in close proximity will significantly suppress the reactor $\bar{\nu}_e$ background down to a negligible level.

6.3.3 Fast neutrons

Cosmic-ray muons or their secondary products may collide with the nuclei in the target or surrounding materials, and knock out energetic fast neutrons. The recoil proton from the fast neutron can mimic a prompt positron signal, while the scattered neutron is quickly thermalized and captured by a nucleus, forming a delayed neutron signal [152].

The fast neutron background was scaled from the KamLAND measurement $(3.2\pm3.2)/(4.53$ kton-year$) = (0.7\pm0.7)$/kton-year [135] to the Jinping site. The muon rate at Jinping is about 1000 times lower than KamLAND, as shown in Fig. 1. As a result, the fast neutron background is reduced to a rather low level, which is estimated to be $(0.7\pm0.7)\times10^{-3}$/kton-year for those with visible energy from 10 to 30 MeV. Here we ignored some minor corrections like the detector shape difference between KamLAND and Jinping, and the fast neutron yield increases as an exponential function of muon energy [153].

6.3.4 Spallation product ^{9}Li/^{8}He

The spallation products ^{9}Li/^{8}He induced by cosmic-ray muons [154] can decay via a beta delayed neutron emission. The beta signal together with the delayed neutron signal have a similar signature to the IBD signal. The half-life and Q-value of ^{9}Li are 173 ms and 14 MeV, respectively, and 119 ms and 11 MeV for ^{8}He, respectively. The visible energy spectra of these two background sources are shown in Fig. 17. It was noted that ^{9}Li/^{8}He backgrounds were usually generated locally and could not fly very far, so that the muons concerned were in the sensitive target region. With an efficient muon detection and new theoretical studies of spallation backgrounds [155, 156], these backgrounds can be effectively removed.

With a suppression factor of 1000 from the large overburden, the KamLAND measurement is scaled to the Jinping case, 4.0/4.53 (kton-year)/1000 = 1×10^{-3}/kton-year, for the visible energy within the range from 10 to 30 MeV.

6.3.5 Atmospheric neutrino CC background

Atmospheric neutrino [157, 158] interactions through the charged current (CC) can form an irreducible background, which is, however, not dominant.

High energy atmospheric $\bar{\nu}_\mu$'s and ν_μ's can produce low-energy muons followed by Michel electrons and delayed neutrons, and contaminate the SRN signal region. In water Cherenkov detectors, the muon momentum can be below the Cherenkov threshold, and become an invisible muon background. However, these muons are always visible in scintillator. Because of the inefficiency of the muon tagging and the negative muon capture, there is still a non-negligible contribution from atmospheric neutrinos.

The rate estimation in KamLAND, 0.9/(4.53 kton-year) = 0.2/kton-year, can be applied to Jinping. With the slow scintillator technique, it was assumed to be 0.1/kton-year with the extra capability of particle identification for both prompt electron and delayed gamma signals.

6.3.6 Atmospheric neutrino NC background

The dominant atmospheric background for SRNs is found to be from the neutral current process (NC) as studied in the KamLAND experiment. Neutrinos at higher energies beyond the signal region may collide with ^{12}C in the target and knock out a neutron. The neutron scattering off protons or particles emitted in the de-excitation of the remaining nuclei causes a prompt signal and the neutron capture will give a delayed signal.

New techniques have been proposed to further suppress this background [150, 159]. To have a delay neutron produced, there is a 2/3 chance that a ^{11}C at ground state is produced. The half-life and Q-value of the ^{11}C ground state are 20 min and 2 MeV, respectively. A triple tagging of the prompt signal, neutron capture, and ^{11}C decay may help to veto this background, but 5% of the background still survives. For the other 1/3 of cases, ^{11}C is in an excited state and decays through neutron, proton or alpha emissions. A pulse shape discrimination technique can also be applied to suppress the background probability down to the 1% level.

It was expected that the background level 16.4/(4.53 kton-year) = 3.6/kton-year at KamLAND could be suppressed roughly by a factor of 16=1/(5%+1%) at Jinping with a background level similar to the CC background of 0.2/kton-year. We expect that in a slow scintillator detector the above level can be further suppressed down to 0.1/kton-year with the extra capability of particle identification.

6.4 SRN Sensitivity

The event rate in $E_{\rm vis}$ for the range around 10–30 MeV are summarized in Table 11, and the results with 3 kton × 3.3 years (10 kton-year) and 3 kton × 6.7 years (20 kton-year) are also shown. With a slow scintillator detector, a neutrino experiment at Jinping is very promising to make a discovery.

7 Dark matter

7.1 Neutrinos from dark matter annihilation in the halo

Neutrinos can be copiously produced via dark matter (DM) annihilation or decay in the Galactic DM halo. For annihilating DM, the resulting neutrino energy spectrum

can be a delta function if the neutrino pair is the direct final state of DM annihilation, i.e. $\chi\chi\to\nu\nu$; or it can also be a continuous one, if DM annihilates into Standard Model fermions which subsequently decay with neutrinos. In this section, we will focus on the case where the neutrino spectrum is a delta function, since the monoenergetic neutrinos are readily distinguished from the background. The differential flux of the anti-electron-neutrino in the $\chi\chi\to\nu\nu$ case is given by (neglecting neutrino oscillations)

$$\frac{\mathrm{d}\phi_{\bar{\nu}_e}(E_{\bar{\nu}_e}=m_\chi,\psi)}{\mathrm{d}\Omega}=\frac{1}{2}\frac{\langle\sigma_{\chi\chi\to\nu\nu}v\rangle}{4\pi m_\chi^2}\frac{1}{3}\int_{\rm los}\mathrm{d}x\rho_\chi^2(r(x,\psi))$$
$$\equiv\frac{\langle\sigma_{\chi\chi\to\nu\nu}v\rangle}{24\pi m_\chi^2}J(\psi), \tag{27}$$

where the factor (1/3) averages over the three flavors, the factor (1/2) pertains to identical DM particles, the integral is carried out along the line of sight (los), $\rho_\chi(m_\chi)$ is DM density (mass), ψ is the angle away from the galactic center (GC), Ω indicates the direction of DM annihilation, $r(x,\psi)=(x^2+R_\odot^2-2xR_\odot\cos(\psi))^{1/2}$ is the distance to the GC, $R_\odot=8.5$ kpc is the distance from the GC to the solar system, and x is the distance between us and the location of DM annihilation. For the analysis without any directional information, one can obtain the total anti-electron-neutrino flux

$$\phi_{\bar{\nu}_e}(E_{\bar{\nu}_e}=m_\chi)=\frac{\langle\sigma_{\chi\chi\to\nu\nu}v\rangle}{24\pi m_\chi^2}\int\mathrm{d}\Omega J(\psi)\equiv\frac{\langle\sigma_{\chi\chi\to\nu\nu}v\rangle}{6m_\chi^2}J_{\rm avg}, \tag{28}$$

where $J_{\rm avg}$ is the averaged J factor over the whole sky with a rather weak dependence on the details of the dark matter density distribution in the halo, for some commonly used dark matter profiles: Navarro-Frenk-White (NFW) [160], Moore [161], and Kravtsov [162]. We take the value $J_{\rm avg}/(R_\odot\rho_\odot^2)=5$ [163], assuming $\rho_\odot=0.4$ GeV/cm^3. Thus the anti-electron-neutrino flux at $E_{\bar{\nu}_e}=m_\chi$, is given by

$$\phi_{\bar{\nu}_e}(E_{\bar{\nu}_e}=m_\chi)\simeq 1.1\times10^2\,\mathrm{cm^{-2}\,s^{-1}}\cdot\frac{\mathrm{MeV}^2}{m_\chi^2}\cdot\frac{\langle\sigma_{\chi\chi\to\nu\nu}v\rangle}{3\times10^{-26}\,\mathrm{cm^3\,s^{-1}}} \tag{29}$$

The monoenergetic feature of the neutrinos due to dark matter annihilation considered here makes them quite easy to detect over the continuous backgrounds. The number of events due to the anti-electron-neutrino are given by [164]

$$\mathcal{N}\simeq\sigma_{\rm det}\,\phi_{\bar{\nu}_e}\,N_{\rm target}\,t\,\epsilon, \tag{30}$$

where the detection cross section $\sigma_{\rm det}$ needs to be evaluated at $E_{\bar{\nu}_e}=m_\chi$ for the dark matter annihilation, the total neutrino flux $\phi_{\bar{\nu}_e}$ is given in Eq. (29), $N_{\rm target}$ is the number of target particles in the detector, t is the total time-exposure, and ϵ is the detector efficiency.

The Jinping neutrino experiment can search for monochromatic peaks in the energy range $E\sim(1-100)$ MeV. The dominant backgrounds come from reactors, supernova relics, and atmospheric neutrinos in the energy range of interest. For simplicity, we only consider the DM mass above ~10 MeV with IBD signature, to avoid the reactor neutrino background. The energy resolution is considered to be $\delta E/E=8\%$. The signal events due to DM in the energy bin around the DM mass with bin width equal to twice the energy resolution is computed, which is then compared to the background events to derive the discovery limits. As shown in Fig. 18, one can probe the DM annihilation cross section to $\sim10^{-24}$ (10^{-25}) cm^3/s with 10 (100) kton-year exposure. Current exclusion limits on the DM annihilation into neutrinos are given by KamLAND [135] and Super-Kamiokande [165].

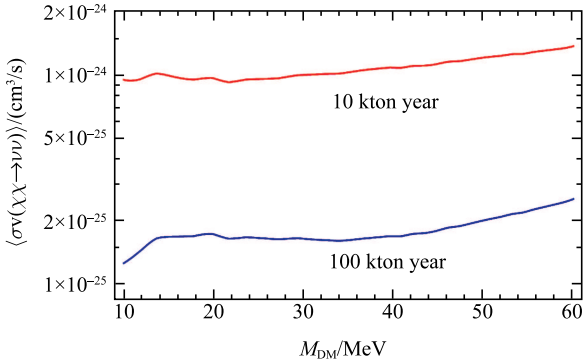

Fig. 18. The discovery reach of the DM annihilation cross section for MeV mass range. The limits is derived with criteria $S=5\sqrt{B}$ or 10 events, whichever is larger. Three backgrounds: supernova relic neutrino, atmospheric neutrino (both CC and NC) are considered. We assume 100% detection efficiency here.

7.2 Neutrinos from dark matter annihilation in the Sun

Another promising signal for indirect detection of dark matter is to look for energetic neutrinos from the annihilation of dark matter that have accumulated in the Sun and/or Earth (for early discussions, see e.g. [166–170]). When the solar system moves through the dark matter halo, a dark matter particle can scatter off a nucleus in the Sun or Earth and lose its velocity to be lower than the escape velocity, and thus becomes gravitationally trapped. The dark matter particle undergoes various scatterings in the Sun and eventually settles to the core, after capture. Over the lifetime of the Sun, a sufficient amount of dark matter can accumulate in the core, so an equilibrium between capture and annihilation (or evaporation) is expected. Unlike other Standard

Model particles, the neutrinos produced via dark matter annihilation can escape easily from the Sun and can be detected in neutrino experiments on the Earth. The number of dark matter particles inside the Sun, N_χ, is described by the differential equation

$$\frac{\mathrm{d}N_\chi}{\mathrm{d}t} = C_\mathrm{C} - C_\mathrm{A}N_\chi^2 - C_\mathrm{E}N_\chi, \tag{31}$$

where the three constants describe capture (C_C), annihilation (C_A), and evaporation (C_E). For dark matter heavier than the evaporation mass (which is typically 3–4 GeV [171, 172]), the C_E term can be ignored. The dark matter annihilation rate is given by [173]

$$\Gamma_\mathrm{A} \equiv \frac{1}{2C_\mathrm{A}N_\chi^2} = \frac{1}{2}C_\mathrm{C}\tanh^2(t/\tau), \tag{32}$$

where $\tau \equiv 1/\sqrt{C_\mathrm{C}C_\mathrm{A}}$. The present dark matter annihilation rate is found for $t = t^\odot \simeq 4.5\times10^9$ years. When $t^\odot \gg \tau$, the annihilation and capture are in equilibrium, so one has $\Gamma_\mathrm{A} = C_\mathrm{C}/2$. Thus, in equilibrium, the Γ_A only depends on the capture rate. Therefore, the resulting neutrino flux depends on the dark matter-nucleus cross section in the capture process, not on the annihilation cross section. The dark matter spin-dependent cross section, σ^SD, can be written as [173, 174]

$$\sigma^\mathrm{SD} = \kappa_f^\mathrm{SD}(m_\chi)\phi_\mu^f \tag{33}$$

where $\kappa_f^\mathrm{SD}(m_\chi)$ is the conversion factor between the spin-dependent cross section and the muon flux. The $\kappa_f^\mathrm{SD}(m_\chi)$ can be obtained from Figure 3 of Ref. [173] for the Standard Model final states, $f = W^+W^-, \tau^+\tau^-, t\bar{t}, b\bar{b}$, from which the neutrinos come. These curves are based on calculations using DarkSUSY [175]. The Super-Kamiokande [176] experiment has the best constraint on the dark matter spin-dependent cross section from neutrino telescope experiments.

7.3 Discussion

Beside high energy neutrinos from the annihilation of dark matter particles, low energy neutrinos can also be considered [177, 178]. Searches for neutrinos from the dark matter annihilations in the Sun and halo are possible with the Jinping neutrino experiment; however, the target mass is still a limiting factor for the final sensitivity. Liquid scintillator or water-based liquid scintillator detectors will have a higher efficiency than water detectors at tens of MeV. If the direction information is available with the slow liquid scintillator, the sensitivity may be further enhanced. More studies on this topic are in progress.

8 Summary

The China Jinping Underground Laboratory, with its extremely low cosmic-ray muon flux and low reactor neutrino flux, is an ideal site to do low background neutrino experiments. With a 2000-ton fiducial mass for solar neutrino physics (equivalently, 3000 tons for geo-neutrino and supernova relic neutrino physics), we find that Jinping should be able to discover the neutrinos from the CNO fusion cycles of the Sun, to precisely measure the transition phase for solar neutrino oscillation from the vacuum to the matter effect, to precisely determine the geo-neutrino flux and the U, Th ratio, and to help determine the geo-neutrino models. It will bring our knowledge of these areas to a brand new stage. These physics goals can be fulfilled with existing mature techniques. Efforts on increasing the target mass with multi-modular neutrino detectors and developing the slow scintillator technique will enable us to eventually enrich the Jinping discovery potential. With the deepest motivation and wish to explore the Sun, the Earth, the universe, and the smallest fundamental particle – the neutrino – we propose a neutrino experiment at Jinping.

We acknowledge Tsinghua University (THU) and Yalong River Hydropower Development Company, Ltd. (Yalong Hydro) for building the underground laboratory and continuing efforts on the future development and maintenance of the CJPL.

References

1 http://jinping.hep.tsinghua.edu.cn
2 K. J. Kang et al, Journal of Physics: Conference Series **203**: 012028 (2010)
3 Q. Yue et al, Phys. Rev. D (R), **90**: 091701 (2014)
4 M. J. Xiao et al, Sci China-Phys Mech Astron, **57**: 2024 (2014)
5 Jianmin Li, Xiangdong Ji, Wick Haxton, and Joseph S.Y. Wang, Physics Procedia, **61**: 576 (2015)
6 Ke-Jun Kang et al, Front. Phys., **8(4)**: 412 (2013)
7 F. Duncan, A. J. Noble, and D. Sinclair, Annu. Rev. Nucl. Part. Sci., **60**: 163 (2010)
8 C. Arpesella, Appl. Radiat. Isot. **47**: 991, (1996)
9 Precision Measurement of Neutrino Oscillation Parameters and Investigation of Nuclear Georeactor Hypothesis with KamLAND, Chao Zhang, PhD. Thesis, California Institute of Technology (2011)
10 Y. C. WU, Chinese Phys. C, **37**: 086001 (2013)
11 Corey Adams et al (LBNE Collaboration), arXiv:1307.7335 (2013)
12 International Atomic Energy Agency, http://www.iaea.org/ (2015)
13 M. Yeh et al, Nucl. Instrum. Methods. A, **51**: 660 (2011)
14 J. R. Alonso et al, arXiv:1409.5864v3 (2014)
15 M. H. Li et al, Nucl. Instrum. Methods. A, **830**: 303 (2016)
16 S. Agostinelli et al, Nuclear Instruments and Methods in Physics Research A, **506**: 250 (2003)
17 J. Allison et al, IEEE Trans. Nucl. Sci., **53**: 270 (2006)

18 J. Bahcall, SLAC Beam Line 31N1, 2-12 (2001) [arXiv:astro-ph/0009259 (2000)]
19 W.C. Haxton, Nature, **512**: 378 (2014)
20 A.B. McDonald, New Journal of Physics, **6**: 121 (2004)
21 Solar neutrinos the first thirty years, edited by J. Bahcall, et al, Westview Press (1994)
22 J. Bahcall home page: http://www.sns.ias.edu/˜jnb/
23 A. Serenelli, Eur. Phys. J. A, **52**: 78 (2016)
24 Neutrino Astrophysics, J. Bahcall, Cambridge University Press (1989)
25 W.C. Haxton, R.G. and A. Serenelli, Astrophys. J. **687**: 678 (2008)
26 A. Serenelli, C. Peña-Garay, and W.C. Haxton, Phys. Rev. D, **87**: 043001 (2013)
27 E.G. Adelberger et al, Rev. Mod. Phys., **70**: 1265 (1998)
28 E.G. Adelberger et al, Rev. Mod. Phys., **83**: 195 (2011)
29 Home page of LUNA: http://luna.lngs.infn.it/
30 Home page of JUNA: http://www.juna.ac.cn/
31 W. Liu et al, Nuclear Physics A, **616**: 131 (1997)
32 B. Pontecorvo, Sov. Phys. JETP, **6**: 429 (1957) and **26**: 984 (1968)
33 Z. Maki, M. Nakagawa, and S. Sakata, Prog. Theor. Phys., **28**: 870 (1962)
34 L. Wolfenstein, Phys. Rev. D, **17**: 2369 (1978)
35 S.P. Mikheev and A.Y. Smirnov, Sov. J. Nucl. Phys., **42**: 913 (1985); Nuovo Cimento, **9C**: 17 (1986)
36 B.T. Cleveland et al, Astrophys. J. **496**: 505 (1998)
37 J.N. Abdurashitov et al (SAGE Collaboration), Phys. Rev. C, **80**: 015807 (2009)
38 P. Anselmann et al (GALLEX Collaboration), Phys. Lett. B, **285**: 376 (1992)
39 M. Altmann et al (GNO Collaboration), Phys. Lett. B, **616**: 174 (2005)
40 Y. Fukuda et al (Kamiokande Collaboration), Phys. Rev. Lett., **77**: 1683 (1996)
41 S. Fukuda et al (Super-Kamiokande Collaboration), Phys. Lett. B, **539**: 179 (2002)
42 Q.R. Ahmad et al (SNO Collaboration), Phys. Rev. Lett., **89**: 011301 (2001)
43 G. Bellini et al (Borexino Collaboration), Phys. Rev. D, **89**: 112007 (2014)
44 R.B. Leighton, R.W. Noyes, and G.W. Simon, Astrophys. J. **135**: 474 (1962)
45 W.C. Haxton, R.G. Hamish Robertson, and A. Serenelli, Annu. Rev. Astron. Astrophys., **51**: 21 (2013)
46 J. Bahcall and C. Peña-Garay, New J. of Phys., **6**: 63 (2004)
47 J. Bahcall and R. K. Ulrich, Rev. Mod. Phys., **60**: 297 (1988)
48 J. Bahcall and C. Peña-Garay, JHEP, **11**: 004 (2003)
49 A. Serenelli et al, Astrophys. J. **705**: L123 (2009)
50 A. Serenelli, W. C. Haxton, and C. Peña-Garay, Astrophys. J. **743**: 24 (2011)
51 P. C. de Holanda and A. Yu. Smirnov, Phys. Rev. D **69**: 113002 (2004)
52 R. Bonventre et al, Phys. Rev. D, **88**: 053010 (2013)
53 A. Friedland, C. Lunardini, and C. Peña-Garay, Phys. Lett. B, **594**: 347 (2004)
54 M. Maltoni and A. Yu. Smirnov, Eur. Phys. J. A, **52**: 87 (2016)
55 K. Abe, et al (Super-Kamiokande Collaboration), Phys. Rev. D, **94**: 052010 (2016)
56 S. Abe, et al (KamLAND Collaboration), Phys. Rev. L, **100**: 221803 (2008)
57 J. N. Bahcall and P. I. Krastev, Phys. Rev. C. **56**: 2839 (1997)
58 J. N. Bahcall, P. I. Krastev, and A. Yu. Smirnov, Phys. Rev. D. **60**: 093001 (1999)
59 A. Renshaw et al, Phys. Rev. Lett.. **112**: 091805 (2014)
60 A. Serenelli, S. Basu, J.W. Ferguson, and M. Asplund, Astrophys. J. **705**: L123 (2009)
61 J. Bahcall, A. Serenelli, and S. Basu, Astrophys. J. Suppl. Ser., **165**: 400 (2006)
62 S. J. Park, Phys. Rev. Lett., **57**: 1275 (1986)
63 W. C. Haxton, Phys. Rev. Lett., **57**: 1271 (1986)
64 P. C. de Holanda, Wei Liao, and A. Yu. Smirnov, Nucl. Phys. B, **702**: 307 (2004)
65 J. Bahcall, M. H. Pinsonneault, and S. Basu, Astrophys. J. **555**: 990 (2001)
66 G. L. Fogli, E. Lisi, D. Montanino, and A. Palazzo1, Phys. Rev. D, **62**: 113004 (2000)
67 E. Lisi, A. Marrone, D. Montanino, A. Palazzo, and S. T. Petcov, Phys. Rev. D, **63**: 093002 (2000)
68 S. Goswami and A. Y. Smirnov, Phys. Rev. D, **72**: 053011 (2005)
69 C. Giunti and C. W. Kim, Fundamentals of Neutrino Physics and Astrophysics, Oxford University Press (2007)
70 B. Aharmim, et al (SNO Collaboration) Phys. Rev. C, **72**: 055502 (2005)
71 L. Oberauera, C. Grieba, F. Feilitzscha, and I. Mannoc, Nucl. Instr. and Meth. A, **530**: 453 (2004)
72 K. Abe, et. al. (Super-Kamiokande Collaboration), Phys. Rev. D **83**: 052010 (2011)
73 C. Arpesella et al (Borexino Collaboration), Phys. Rev. Lett., **101**: 091302 (2008)
74 G. Bellini et al (Borexino Collaboration), Phys. Rev. Lett., **107**: 141302 (2011)
75 G. Bellini et al (Borexino Collaboration), Phys. Rev. Lett., **108**: 051302 (2012)
76 G. Bellini et al (Borexino Collaboration), Phys. Rev. D, **82**: 033006 (2010)
77 G. Bellini et al (Borexino Collaboration), Nature, **512**: 383 (2014)
78 B. Aharmim et al (SNO Collaboration), Phys. Rev. C, **88**: 025501 (2013)
79 F. P. An et al (Daya Bay Collaboration), Phys. Rev. Lett., **112**: 061801 (2014)
80 Jia-Hua Cheng et al, Nucl. Instr. and Meth. A, **827**: 165 (2016)
81 O.G. Miranda, M.A. Tórtola, and J.W.F. Valle, JHEP, **10**: 008 (2006)
82 M.C. Gonzalez-Garcia, P.C. de Holanda, E. Masso and R. Zukanovich Funchalc, JCAP, **0806**: 019 (2008)
83 V. Barger, P. Huber, and D. Marfatia, Phys. Rev. Lett., **95**: 211802 (2005)
84 M. Maltoni and A.Y. Smirnov, Eur. Phys. J. A, **52**: 87 (2016)
85 William F. McDonough and Ondřej Šrámek, Environ. Earth Sci. **71**: 3787 (2014)
86 C Jaupart, S Labrosse, and J-C Mareschal, Treatise on geophysics, **7**: 253 (2007)
87 Ondřej Šrámek et al, Earth Planet. Sci. Lett., **361**: 356 (2013)
88 G. Bellini et al, Prog. Part. Nucl. Phys., **73**: 1 (2013)
89 Ondřej Šrámek et al, Sci. Rep., **6**: 33034 (2016)
90 T. Araki et al (KamLAND Collaboration), Nature, **436**: 499 (2005)
91 A. Gando et al (KamLAND Collaboration), Nature Geoscience, **4**: 647 (2011)
92 A. Gando et al (KamLAND Collaboration), Phys. Rev. D, **88**: 033001 (2013)
93 G. Bellini et al (Borexino Collaboration), Phys. Lett. B, **687**: 299 (2010)
94 G. Bellini et al (Borexino Collaboration), Phys. Lett. B, **722**: 295 (2013)
95 M. Agostini et al (Borexino Collaboration), Phys. Rev. D, **92**: 031101(R) (2015)
96 Y. Huang et al, Geochem. Geophys. Geosyst., **14**: 2003 (2013).
97 C. Bassin, G. Laske, and T. G. Masters (2000), The current limits of resolution for surface wave tomography in North America, *EOS Trans.*
98 N. M. Shapiro, and M. H. Ritzwoller, Geophysical Journal International, **151**: 88 (2002)

99 M. Negretti, M. Reguzzoni, and D. Sampietro, A web processing service for GOCE data exploitation, in First International GOCE Solid Earth workshop, edited, Enschede, The Netherlands (2012)
100 Y. Huang, V. Strati, F. Mantovani, S. B. Shirey, and W. F. McDonough, Geochem. Geophys. Geosyst., **15**: 3925 (2014)
101 D. F. Hollenbach and J. M. Herndon, Proc. Nat. Acad. Sci., **98**: 11085 (2001)
102 S. Enomoto, Neutrino geophysics and observation of geoneutrinos at KamLAND, Ph.D. Thesis, Tohoku University (2005)
103 P. Vogel and J. F. Beacom, Phys. Rev. D, **60**: 053003 (1999)
104 X. B. Ma et al, Phys. Rev. C, **88**: 014605 (2013)
105 International Atomic Energy Agency, http://www.iaea.org/ (2015)
106 M. Baldoncini et al, Phys. Rev. D, **91**: 065002 (2015)
107 K.S. Hirata et al, Phys. Rev. Lett., **58**: 1490 (1987)
108 K.S. Hirata et al, Phys. Rev. D, **38**: 448 (1988)
109 R.M. Bionta et al, Phys. Rev. Lett., **58**: 1494 (1987)
110 C.B. Bratton et al, Phys. Rev. D, **37**: 3361 (1988)
111 E.N. Alekseev et al, JETP Lett., **45**: 589 (1987)
112 E.N. Alekseev et al, Phys. Lett. B, **205**: 209 (1988)
113 G. G. Raffelt, Proc. Int. Sch. Phys. Fermi, **182**: 61 (2012) [arXiv:1201.1637]
114 R.N. Mohapatra and P.B. Pal, *Massive Neutrinos in Physics and Astrophysics*, World Scientific Publishing Co. Pte. Ltd. 2004
115 C. Lunardini and A.Y. Smirnov, JCAP, **0306**: 009 (2003)
116 P.D. Serpico, S. Chakraborty, T. Fischer et al, Phys. Rev. D, **85**: 085031 (2012)
117 C.D. Ott, E.P. O'Connor, S. Gossan et al, Nucl. Phys. B (Proc. Suppl.), **235-236**: 381 (2013)
118 S. Ando, J.F. Beacom, H. Yüksel, Phys. Rev. Lett., **95**: 171101 (2005)
119 SNEWS, *http://snews.bnl.gov (2015)*, *Supernova Early Warning System*
120 K. Scholberg et al, New J. Phys., **6**: 114 (2004)
121 S. M. Adams et al, J. Astrophys., **778**: 164 (2013)
122 G. Raffelt, I. Tamborra, B. Müller and L. Hüdepohl and H.T. Janka, Phys. Rev. D, **86**: 125031 (2012)
123 K. Scholberg, Annu. Rev. Nucl. Part. Sci. **62**: 81 (2012)
124 John F. Beacom, Will M. Farr and Petr Vogel, Phys. Rev. D, **66**: 033001 (2002)
125 Basudeb Dasgupta and John F. Beacom, Phys. Rev. D, **83**: 113006 (2011)
126 B. von Krosigk et al, Eur. Phys. J. C, **73**: 2390 (2013)
127 Hanyu Wei et al, Astropart. Phys., **75**: 38 (2016)
128 F. P. An et al (Daya Bay Collaboration), Phys. Rev. D (R), **90**: 071101 (2014)
129 F. P. An et al (Daya Bay Collaboration), Phys. Rev. D, **93**: 072011 (2016)
130 M. Ikeda et al (Super-Kamiokande Collaboration), Astrophys. J. **669**: 519 (2007)
131 John F. Beacom and P. Vogel, Phys. Rev. D, **60**: 033007 (1999)
132 M. Malek et al (Super-Kamiokande Collaboration), Phys. Rev. Lett., **90**: 061101 (2003)
133 K. Bays et al (Super-Kamiokande Collaboration), Phys. Rev. D, **85**: 052007 (2012)
134 H. Zhang et al (Super-Kamiokande Collaboration), Astropart. Phys., **60**: 41 (2015)
135 A. Gando et al (KamLAND Collaboration), Astrophys. J. **745**: 193 (2012)
136 G. Bellini et al (Borexino Collaboration), Phys. Lett. B, **696**: 191 (2011)
137 B. Aharmim et al (SNO Collaboration), Astrophys. J. **653**: 1545 (2006)
138 J. F. Beacom, Annu. Rev. Nucl. Part. Sci., **60**: 439 (2010)
139 S. Ando, K. Sato and T. Totani, Astropart. Phys., **18**: 307 (2003); J. Phys. Soc. Jpn. (Suppl. B), **77**: 9 (2008)
140 T. Totani and K. Sato, Astropart. Phys., **3**: 367 (1995)
141 R. A Malaney, Astropart. Phys., **7**: 125 (1997)
142 D. H. Hartmann and S. E. Woosley, Astropart. Phys., **7**: 137 (1997)
143 M. Kaplinghat, G. Steigman and T. P. Walker, Phys. Rev. D, **62**: 043001 (2000)
144 L. Strigari, M. Kaplinghat, G. Steigman and T. Walker, JCAP, **0403**: 007 (2004)
145 T. Totani, K. Sato and Y. Yoshii, Astrophys. J. **460**: 303 (1996)
146 S. Horiuchi, J. F. Beacom and E. Dwek, Phys. Rev. D, **79**: 083013 (2009)
147 M. Fukugita and M. Kawasaki, Mon. Not. Roy. Astron. Soc., **340**: L7 (2003)
148 C. Lunardini, Phys. Rev. Lett., **102**: 231101 (2009)
149 J. F. Beacom and M. R. Vagins, Phys. Rev. Lett., **93**: 171101 (2004)
150 M. Wurm, Astropart. Phys., **35**: 685 (2012)
151 Jingyi Yu, Zhe Wang, and Shaomin Chen, Chin. Phys. C, **39**: 056102 (2015)
152 F. P. An et al (Daya Bay Collaboration), Chin. Phys. C, **37**: 011001 (2013)
153 S. Abe et al (KamLAND Collaboration), Phys. Rev. C, **81**: 025807 (2010)
154 Shirley Weishi Li and John F. Beacom, Phys. Rev C, **89**: 045801 (2014)
155 Shirley Weishi Li and John F. Beacom, Phys. Rev. D, **92**: 105033 (2015)
156 Shirley Weishi Li and John F. Beacom, Phys. Rev. D, **91**: 105005 (2015)
157 O. Peres and A. Smirnov, Phys. Rev. D, **79**: 113002 (2009)
158 G. Battistoni, A. Ferrari, T. Montaruli and P.R. Sala, Astropart. Phys., **23**: 526 (2005)
159 R. Moellenberg, Ph. D. thesis, Technische Universität München (2009)
160 J. F. Navarro, C. S. Frenk and S. D. M. White, Astrophys. J. **462**: 563 (1996)
161 B. Moore, T. R. Quinn, F. Governato, J. Stadel and G. Lake, Mon. Not. Roy. Astron. Soc., **310**: 1147 (1999)
162 A. V. Kravtsov, A. A. Klypin, J. S. Bullock and J. R. Primack, Astrophys. J. **502**: 48 (1998)
163 H. Yuksel, S. Horiuchi, J. F. Beacom and S. Ando, Phys. Rev. D, **76**: 123506 (2007)
164 M. Wurm et al (LENA Collaboration), Astropart. Phys., **35**: 685 (2012)
165 S. Palomares-Ruiz and S. Pascoli, Phys. Rev., D **77**: 025025 (2008)
166 J. Silk, K. A. Olive and M. Srednicki, Phys. Rev. Lett., **55**: 257 (1985)
167 L. M. Krauss, K. Freese, W. Press and D. Spergel, Astrophys. J. **299**: 1001 (1985)
168 K. Freese, Phys. Lett. B, **167**: 295 (1986)
169 L. M. Krauss, M. Srednicki and F. Wilczek, Phys. Rev. D, **33**: 2079 (1986)
170 T. K. Gaisser, G. Steigman and S. Tilav, Phys. Rev. D, **34**: 2206 (1986)
171 K. Griest and D. Seckel, Nucl. Phys. B, **283**: 681 (1987) [Erratum-ibid. B, **296**: 1034 (1988)]
172 A. Gould, Astrophys. J. **321**: 560 (1987)
173 G. Wikstrom and J. Edsjo, JCAP, **0904**: 009 (2009)
174 T. Tanaka et al (Super-Kamiokande Collaboration), Astrophys. J. **742**: 78 (2011)
175 P. Gondolo, J. Edsjo, P. Ullio, L. Bergstrom, M. Schelke and E. A. Baltz, JCAP, **0407**: 008 (2004)
176 K. Choi et al (Super-Kamiokande Collaboration), Phys. Rev. Lett., **114**: 141301 (2015)
177 Nicolás Bernal, Justo Martín-Albo and Sergio Palomares-Ruiz, JCAP, **1308**: 011 (2013)
178 Carsten Rott, Jennifer M. Siegal-Gaskins, and John F. Beacom, Phys. Rev. D, **88**: 055005 (2013)